Peer review status:

This is a non-peer-reviewed preprint submitted to EarthArXiv.

This is a non-peer reviewed pre-print submitted to EarthArXiv. Subsequent versions of this manuscript may have slightly different content. The manuscript has been submitted to International Journal of Greenhouse Gas Control for peer-review.

Fourier Neural Operator Surrogates for Hysteretic Multiphase Flow in Heterogeneous Geological CO_2 Storage Reservoirs

B. Venkateshwaran[1, 2*], AKM Eahsanul Haque[1,2,3], Numair Ahmed Siddiqui[1], Hariharan Ramachandran[4], M. Ramkumar[5], John Oluwadamilola Olutoki[6], Ida Bagus Suananda Yogi[1, 2], Bamidele Adeniyi[1, 2]

[1] Department of Geoscience, Universiti Teknologi PETRONAS, Bandar Seri Iskandar 32610, Perak, Malaysia.
[2] Centre for Subsurface Imaging, Institute of Hydrocarbon Recovery, Universiti Teknologi PETRONAS, Seri Iskandar 32610, Malaysia.
[3] Physics & Astronomy Division, SETI Institute, CA USA.
[4] Institute of GeoEnergy Engineering (IGE), Heriot-Watt University, Edinburgh, UK.
[5] Department of Geology, Periyar University, Salem 636011, India.
[6] Department of Geophysics, University of Queensland, Australia

[*]**Corresponding author and email: venkateshwa_22011656@utp.edu.my and venkateshwarangeo@gmail.com**

Fourier Neural Operator Surrogates for Hysteretic Multiphase Flow in Heterogeneous Geological CO_2 Storage Reservoirs

B. Venkateshwaran[1, 2*], AKM Eahsanul Haque[1,2,3], Numair Ahmed Siddiqui[1], Hariharan Ramachandran[4], M. Ramkumar[5], John Oluwadamilola Olutoki[6], Ida Bagus Suananda Yogi[1, 2], Bamidele Adeniyi[1, 2]

[1] Department of Geoscience, Universiti Teknologi PETRONAS, Bandar Seri Iskandar 32610, Perak, Malaysia.
[2] Centre for Subsurface Imaging, Institute of Hydrocarbon Recovery, Universiti Teknologi PETRONAS, Seri Iskandar 32610, Malaysia.
[3] Physics & Astronomy Division, SETI Institute, CA USA.
[4] Institute of GeoEnergy Engineering (IGE), Heriot-Watt University, Edinburgh, UK.
[5] Department of Geology, Periyar University, Salem 636011, India.
[6] Department of Geophysics, University of Queensland, Australia

[*]Corresponding author and email: venkateshwa_22011656@utp.edu.my and venkateshwarangeo@gmail.com

ABSTRACT

Modeling hysteresis in heterogeneous field-scale reservoirs is essential for estimating residual CO_2 trapping capacity and assessing the security of geological storage. This requires accounting for both relative permeability hysteresis and capillary pressure hysteresis, which control path-dependent multiphase flow and the spatial distribution of trapped gas. Because maximum residual gas saturation varies across lithofacies, residual trapping cannot be predicted from saturation alone when reservoir properties are spatially discontinuous. However, full-physics hysteresis-enabled simulations are computationally expensive, making large-scale storage appraisal impractical. To address this challenge, we develop 2D Fourier Neural Operator (FNO) surrogates that predict CO_2 and brine saturation fields together with a hysteresis states. The models are evaluated across three complexity levels: Case F, a homogeneous system; Case D, a heterogeneous system with variable porosity and permeability but a single trapping law; and Case M, a multi-lithofacies system with five rock types. Each case is tested under relative permeability-only physics and under coupled relative permeability plus capillary pressure hysteresis. Results show that when trapping behavior is uniform, input fields and flow-condition scalars are sufficient to reproduce saturation evolution with accuracy. In contrast, when residual gas saturation varies

by lithofacies, prediction accuracy deteriorates unless rock type is encoded. Adding a categorical rock-type channel restores performance across all cases, including hysteresis-state classification, but reduces robustness under coarse-to-fine grid transfer. These results show that surrogate modeling of heterogeneous CO_2 storage requires representation of lithofacies-dependent trapping behavior. Petrophysical fields alone are insufficient to resolve spatially discontinuous hysteresis physics, especially when capillary pressure hysteresis is included.

Keywords: CO_2 storage; residual trapping; hysteresis; FNO; lithofacies; surrogate modeling.

1. Introduction

Residual trapping through capillary snap-off is one of the most important mechanisms for the long-term immobilization of CO_2 in geological carbon storage reservoirs (Pini et al., 2012; Bolourinejad et al., 2014; Burnside & Naylor, 2014; Krevor et al., 2015; Herring et al., 2016; Kaufmann et al., 2016). In the common water-wet sandstone aquifer setting, CO_2 acts as the non-wetting phase and displaces brine during injection (Benson & Cole, 2008; Newell et al., 2008; Iglauer et al., 2015; Jackson et al., 2018; Reynolds et al., 2018). After injection ceases, buoyancy-driven plume migration is progressively counteracted by brine re-imbibition, which disconnects the CO_2 phase and leaves it trapped as immobile residual ganglia (Bryant et al., 2006; Bech & Frykman, 2018; Rasmusson et al., 2018; Moghadasi et al., 2025). Because residual trapping directly influences storage security, plume persistence, and long-term containment, reliable prediction of this process is essential for assessing the performance of geological carbon storage (Zahasky & Benson, 2014; Dance & Paterson, 2016; Ershadnia et al., 2021; Ni et al., 2021).

Accurate prediction of residual trapping requires multiphase-flow hysteresis, in which relative permeability and capillary pressure depend not only on the current saturation but also on the saturation history (Geffen et al., 1951; Osoba et al., 1951; Jerauld & Salter, 1990; Jerauld, 1997; Element et al., 2003; Akbarabadi & Piri, 2013; Ruprecht et al., 2014; Jin et al., 2018; Zhu et al., 2021; Lan et al., 2024). In practical reservoir simulation, this means that drainage and imbibition branches, scanning curves, and turning-point saturations must be tracked explicitly (Land, 1968; Killough, 1976; Carlson, 1981; Chierici, 1984; Doughty, 2007; Lun & Szafranski, 2023). Hysteresis is therefore not a secondary correction but a fundamental constitutive feature governing post-injection CO_2 redistribution (Doster et al., 2012; Møll Nilsen et al., 2015; Alamara et al., 2023). Experimental and numerical studies have shown that relative permeability hysteresis

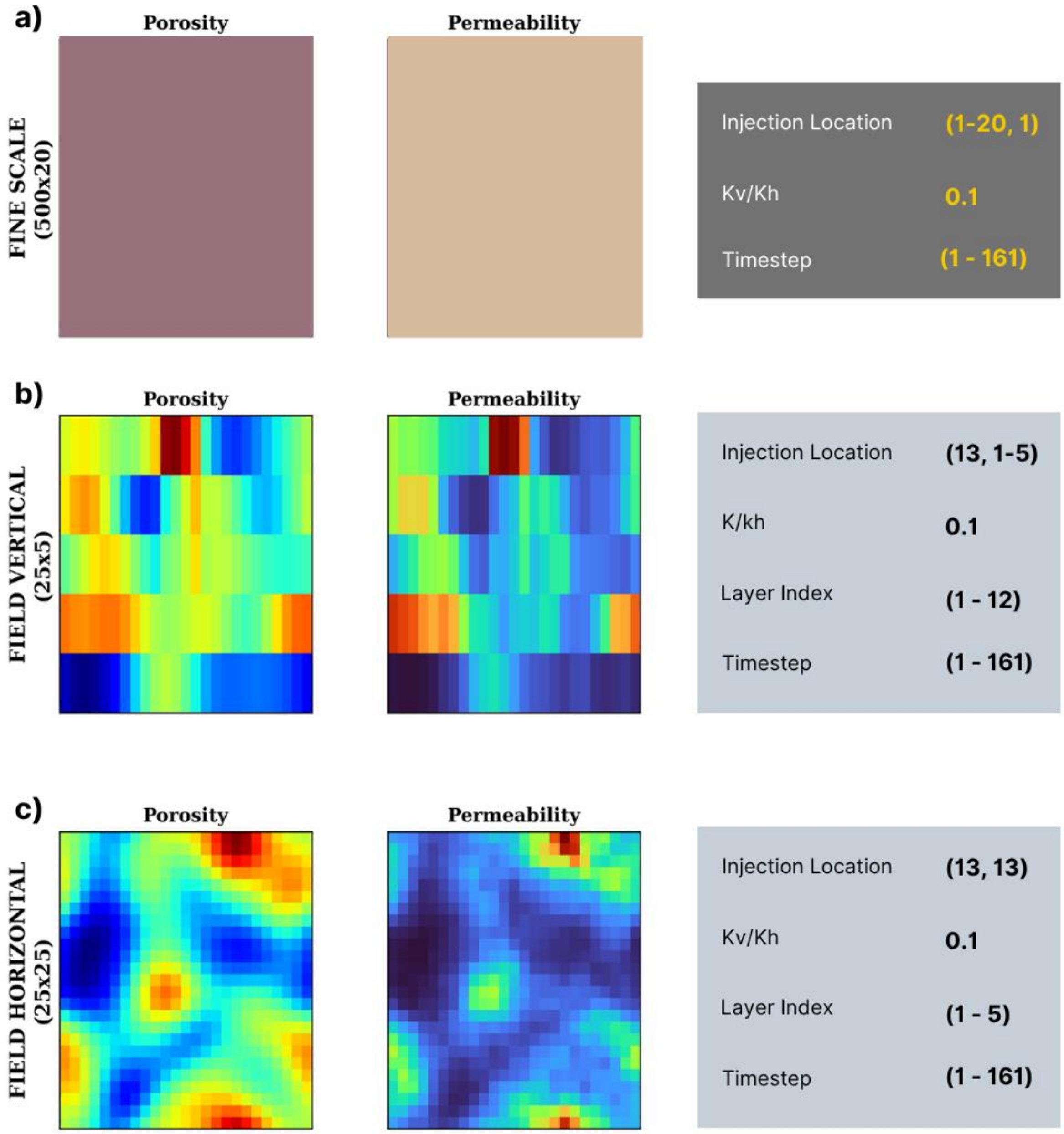

Figure 1: . Input-channel configuration and well placement for the three cases. (a) Case F, a 50 × 1 × 200 vertical section, showing porosity, permeability and the injector indicator. (b) Case D and Case M vertical slices of 25 × 5 cells, indexed 1–25 across the j-direction. (c) Case D and Case M horizontal slices of 25 × 25 cells, indexed 1–5 across the five layers. A single injector operates in every case; no production well is present.

and capillary pressure hysteresis both affect CO_2 trapping behavior (Reynolds & Krevor, 2015; Jackson & Krevor, 2020b; Jackson et al., 2020a; Jettestuen et al., 2021; Jettestuen et al., 2024), and omitting them can alter plume retardation and residual trapping predictions (Juanes et al., 2006; Altundas et al., 2011; Jettestuen et al., 2013). This is why field-scale models that neglect hysteresis may underrepresent both the amount and spatial distribution of trapped CO_2 (Spiteri & Juanes, 2006; Nilsen et al., 2016).

The importance of hysteresis is amplified by geological heterogeneity (Duijn et al., 1995; Doughty & Pruess, 2004; Hovorka et al., 2004; Krevor et al., 2011; Ershadnia et al., 2021). The maximum residual gas saturation varies with rock type and is commonly parameterized using the Land trapping model, which relates trapping capacity to local petrophysical properties such as porosity and permeability (Land, 1968; Holtz, 2002; Krevor et al., 2012; Ni et al., 2019). In heterogeneous reservoirs, different lithofacies can exhibit distinct pore structures, capillary entry pressures, and residual trapping efficiencies; consequently, the distribution of trapped CO_2 reflects both the injection history and the facies architecture (Kumar et al., 2005; Obi & Blunt, 2006; Saadatpoor et al., 2009; Pini et al., 2012; Gershenzon et al., 2015; Gershenzon et al., 2017). Clean, well-connected channel sands may provide large storage capacity but relatively low residual trapping fractions, whereas finer-grained or clay-rich facies often trap a larger fraction of the gas because of their more complex pore networks and stronger capillary effects (Ide et al., 2007; Harris et al., 2021). This is consistent with prior studies showing that heterogeneity and fluvial architecture exert strong control on capillary trapping and residual immobilization in deep saline aquifers (Gershenzon et al., 2015; Ren et al., 2021).

However, incorporating these history-dependent constitutive laws across heterogeneous domains is computationally expensive (Ashraf et al., 2013; Wen et al., 2021a). High-resolution multiphase simulations with hysteresis require substantial computational resources, especially when applied to field-scale scenarios, long post-injection periods, or ensemble-based uncertainty studies (Frangos et al., 2010; Alqahtani et al., 2023). This cost becomes a major bottleneck for practical storage appraisal and uncertainty quantification, making brute-force numerical forecasting impractical for many applications (Wen et al., 2021a). This computational limitation has motivated increasing interest in reduced-order and data-driven surrogate models for CO_2 storage, particularly for large-scale screening and long-term forecasting (Tahmasebi et al., 2020; Sun et al., 2021; Tang et al., 2021; Tang et al., 2022).

Data-driven surrogate models provide a promising alternative (Wen et al., 2021a). Conventional convolutional neural network (CNN) approaches have been used to accelerate subsurface flow prediction, but they are often constrained by grid-dependent architectures and require large training datasets (Wen et al., 2021b; Xiao et al., 2023; Feng et al., 2025a, 2025b, 2026). Fourier Neural Operators (FNOs) address these limitations by learning mappings between function spaces, offering improved data efficiency, lower inference cost, and discretization-invariant prediction across spatial resolutions not explicitly seen during training (Li et al., 2021; Choubineh et al., 2023; Kovachki et al., 2023). In the context of CO_2 storage, FNO-based surrogates have been used to predict plume migration during injection and, more recently, during both injection and post-injection periods (Wen et al., 2022; Yan et al., 2022). Recent work has also demonstrated the potential of FNO-based surrogates for realistic geologies, real-time high-resolution storage prediction, and large-scale multiphase flow acceleration (Jiang et al., 2023; Wen

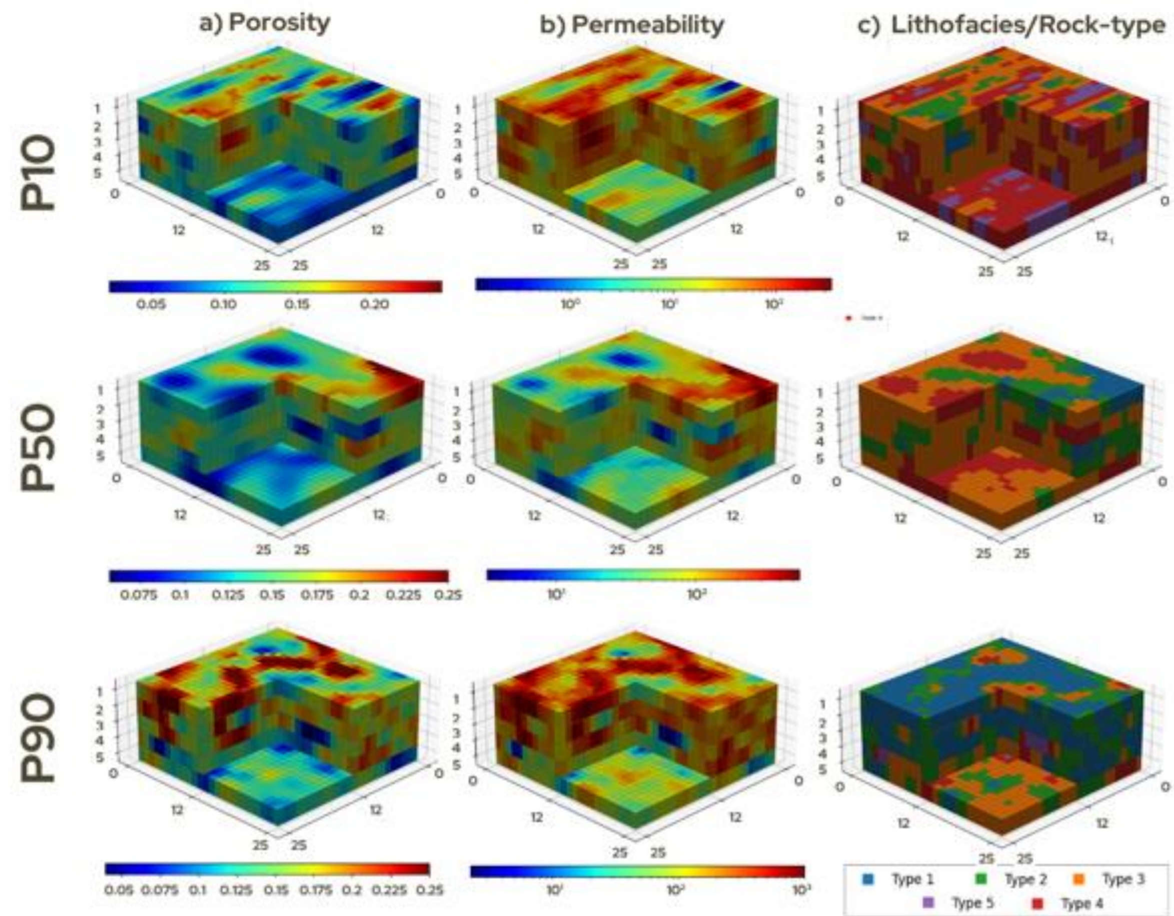

Figure 2: Three-dimensional property distributions for Case D and Case M across the P10, P50 and P90 scenarios. (a) Porosity (fraction). (b) Permeability (log10 mD). (c) Rock-type classification, Case M only (RT1–RT5). Top row, P10, dominated by RT3 and RT4; middle row, P50, balanced; bottom row, P90, dominated by RT1 and RT2. Panels (a) and (b) also document the input fields of a single realization.

et al., 2023). However, most existing surrogate models still rely on simplified constitutive descriptions, commonly assuming spatially homogeneous saturation functions and neglecting lithofacies-dependent hysteresis (Han et al., 2024; Tariq et al., 2024). As a result, they cannot yet represent residual trapping with sufficient physical fidelity in heterogeneous reservoirs (Witte et al., 2023).

Table 1: Summary of model configurations. For each case the table gives the grid dimensions, the number of realizations, the porosity and permeability ranges, the number of rock types, the input channels, the physics settings (RP and RPC) and the slice orientations. Vertical slices are the 25 cross-sections of 25 × 5 cells; horizontal slices are the five layers of 25 × 25 cells. Every configuration is trained with all three architectures over the injection, post-injection and combined scenarios.

Case	Grid	Real.	Scenario / Rock Type	Porosity (–)	Permeability (mD)	*Sgr,max*	Orientation
Case F	50x1x200	50	P10	0.100–0.118	15–34	0.30 (uniform)	Vertical
			P50	0.132–0.150	59–93	0.30 (uniform)	
			P90	0.135–0.154	66–116	0.30 (uniform)	
Case D-RP, D-RPC	25x25x5	90	P10	0.100–0.119	0–662	0.30 (uniform)	Vertical (25x5); Horizontal (25x25)
			P50	0.130–0.149	0–924	0.30 (uniform)	
			P90	0.136–0.155	0–979	0.30 (uniform)	
Case M-RP, M-RPC	25x25x5	90	RT1 Channel Sand	0.157–0.250	200–979	0.12	Vertical (25x5); Horizontal (25x25)
			RT2 Clean Sand	0.130–0.233	100–200	0.18	
			RT3 Silty Sand	0.091–0.195	30–100	0.25	
			RT4 Silt	0.060–0.139	5–30	0.32	
			RT5 Shale	0.001–0.080	< 5	0.38	

To address this gap, this study develops a Fourier Neural Operator-based surrogate framework trained on hysteresis-enabled numerical simulations across multiple levels of geological complexity, including a fine-scale 2D model (Case F), a field-scale 3D model (Case D), and a multi-field-scale 3D model (Case M). Three neural operator architectures are evaluated: the standard FNO, Adaptive FNO (AFNO), and U-FNO (Li et al., 2021; Guibas et al., 2022; Wen et al., 2022). The proposed framework is designed to predict temporally evolving CO_2 saturation fields while simultaneously classifying the local hysteresis state of each grid cell, thereby embedding both saturation dynamics and path-dependent flow behavior into the surrogate model. By combining geological heterogeneity with hysteresis-aware learning, this work aims to provide a computationally efficient and physically consistent tool for long-term CO_2 storage prediction.

2. Methodology

The surrogate modeling workflow is organized into a three-case hierarchy of increasing geological complexity (Table 1). Case F is a fine-scale two-dimensional model that isolates the baseline hysteretic behavior in a homogeneous rock. Case D is a field-scale three-dimensional model that adds spatially varying porosity and permeability while retaining a single trapping law (a single, homogeneous rock type). Case M shares the Case D grid but assigns five rock types, each with its own trapping law. Cases D and M share the same geometry and fluid system and differ only in the number of rock types, so the effect of rock-type heterogeneity is isolated. All 230 realizations were generated with the CMG-GEM compositional simulator.

2.1 Geological setting and property sampling

Each realization represents a synthetic fluvial-channelized reservoir typical of a deep clastic saline formation. The porosity field is generated as a spatially correlated Gaussian random field, obtained by convolving a zero-mean, unit-variance Gaussian white-noise field with an isotropic smoothing kernel of correlation length 3 to 8 cells laterally and 0.5 to 2 cells vertically, then rescaling the smoothed field to the target mean and standard deviation of the scenario being sampled (Table 1). Meandering high-permeability channel bodies and thin low-permeability barriers are superimposed on the smoothed field to reproduce a fluvial depositional architecture. Porosity and permeability in such reservoirs are controlled by primary textural attributes such as grain size and sorting, so the heterogeneity is governed more by sedimentary architecture than by diagenetic overprint (Gershenzon et al., 2015). Permeability is computed from porosity through the modified Kozeny-Carman relation of Eq. 1 (Nooruddin and Hossain, 2011),

$$k = \frac{\phi^3}{(1-\phi)^2} \cdot \frac{d^2}{180\,\tau} \qquad (1)$$

where d is the grain diameter and τ the tortuosity. A grain diameter of 70 to 107 μm and a tortuosity of 2.5 are used, and both are held fixed across the five rock types within a given realization, so lithofacies contrasts arise from the porosity and permeability fields rather than from changes in d or τ. The three scenarios are defined by the mean porosity and mean grain diameter assigned to the Gaussian field before permeability is computed. The percentile (P10) takes the low-porosity, fine-grained end of the range, the median scenario (P50) the central values, and the last percentile scenario (P90) the high-porosity, coarse-grained end. The porosity, permeability and rock-type fields of the three scenarios are shown in Figure 2.

In Case M each cell is assigned one of five rock types (RT1 to RT5) from its local porosity and permeability, following the petrophysical classification used for CO_2 storage screening (Ni et al., 2019). The five types represent a channel sand (RT1), a clean sand (RT2), a silty sand (RT3), a silt (RT4) and a shale (RT5), and each carries its own maximum residual gas saturation and capillary entry pressure (Table 2). Because the assignment applies fixed thresholds in porosity-permeability space, the resulting rock-type field is piecewise constant with sharp contacts between lithofacies.

2.2 Numerical simulation setting

All three cases represent a deep clastic formation with the reservoir top at 2263 m and the initialization datum at 2286 m (Table 1; Figure 1). Case F uses a 50 × 1 × 200 grid representing a vertical cross-section 2.79 km long and 61 m deep, with cells 55.9 m laterally and 0.305 m vertically, which resolves the buoyant rise and the capillary fringe of the plume (Werner et al., 2014). The 3D cases use a 25 × 25 × 5 grid spanning 5.0 km² and 76 m thick, with cells 89.4 m laterally and 15.2 m vertically. The reservoir is initialized at vertical equilibrium under hydrostatic conditions with a pressure of 23.3 MPa at the datum and an isothermal temperature of 93°C. CO_2 is injected for the first 25 years, followed by a 125-year shut-in and monitoring period, yielding a total simulation time of 150 years. The simulation timeline is discretized into 161 report steps, with monthly output during the first year and annual output thereafter, to resolve the rapid pressure response during injection and the slower buoyant relaxation during monitoring. In the 3D cases, the injector is located at the grid center (13,13,1:5) and is operated under a bottomhole pressure cap of 32.8 MPa. Case F uses a single injector along the left boundary, scaled to the smaller domain volume.

The fluid system is modeled as a two-phase CO_2–brine system under water-wet conditions. The formation is initially 100% saturated with resident brine. Dissolution of CO_2 into the aqueous phase is represented using Henry's law (Harvey's correlation for the solubility constant). At reservoir conditions, CO_2 exists as a dense supercritical phase that is less viscous and less dense than brine, driving buoyant plume migration during the monitoring period.

Table 2: Rock-fluid parameters for the synthetic water-wet reservoir: the uniform field rock type used in Cases F and D, and the five Case M rock types RT1–RT5. Columns give the irreducible water saturation, the critical gas saturation, the maximum gas saturation, the endpoint gas and water relative permeabilities, the Corey exponents, the Brooks-Corey entry pressure in kPa, the maximum residual gas saturation and the Land coefficient.

Rock type	S_{wi}	S_{gc}	$S_{g,max}$	$k_{rg,end}$	$k_{rw,end}$	ng	nw	Pe (kPa)	$S_{gr,max}$	Land C
Uniform field	0.16	0.005	0.84	0.858	1.02	2	3.5	12.4	0.3	2.14
RT1 Channel sand	0.16	0.005	0.84	0.86	1.02	2	3	8	0.12	7.14
RT2 Clean sand	0.22	0.005	0.78	0.8	1.02	2.2	3.5	12.89	0.18	4.27
RT3 Silty sand	0.3	0.008	0.7	0.72	1.03	2.5	4	20.29	0.25	2.57
RT4 Silt	0.42	0.012	0.58	0.58	1.03	3	4.5	30.66	0.32	1.4
RT5 Shale	0.55	0.02	0.45	0.45	1.04	3.5	5	42.76	0.38	0.41

2.3 Rock-fluid model and hysteresis

Relative permeability and capillary pressure tables are generated from established empirical models. Table 2 lists the petrophysical parameters for the uniform field rock type and the five rock types RT1-RT5, and Figure 5 shows the resulting saturation functions.

Relative permeability: Gas and water relative permeabilities follow the Corey model on normalized saturations, generated node-by-node in Eqs. 2 and 3:

$$k_{rg} = k_{rg}^{\text{end}}\, S_{eg}^{n_g}, \qquad S_{eg} = \frac{S_g - S_{gc}}{1 - S_{wi} - S_{gc}} \tag{2}$$

$$k_{rw} = k_{rw}^{\text{end}}\, S_{ew}^{n_w}, \qquad S_{ew} = \frac{S_w - S_{wi}}{1 - S_{wi}} \tag{3}$$

where S_{gc} is the critical gas saturation and S_{wi} the irreducible water saturation.

Capillary pressure and hysteresis: Drainage capillary pressure follows the Brooks-Corey model of Eq. 4 (Brooks and Corey, 1964):

$$P_c^{\text{dr}}(S_w) = P_e\, S_{ew}^{-1/\lambda} \tag{4}$$

where Pe is the entry pressure at $S_w = 1$ and λ is the pore-size distribution index. Because Pc diverges as S_w approaches S_{wi} ($S_{ew} = 0$), a numerical floor of $S_{ew} = 0.02$ bounds the maximum drainage Pc, keeping the tables finite and the Newton-Raphson solver stable. The imbibition branch is generated below the drainage branch by scaling it by a constant factor of 0.40. That factor is the condition that keeps both branches monotonic and differentiable at every reversal, which the solver requires (Doughty, 2007). It is a simplification, because measured imbibition branches do not preserve a fixed ratio to the drainage branch (Pini and Benson, 2017; Patel and Meher, 2017), and it therefore fixes only the bounding envelope of Eq. 5:

$$P_c^{\mathrm{imb}}(S_w) = 0.40\, P_c^{\mathrm{dr}}(S_w) \tag{5}$$

which is finite and converges smoothly to zero at the maximum trapped gas saturation. On phase reversal from drainage to imbibition, the residual trapped gas is computed internally by the simulator through the Land (1968) relation of Eqs. 6 and 7 on the historical maximum gas saturation $S_{g,\mathrm{hys}}$:

$$C = \frac{1}{S_{gr,\mathrm{max}}} - \frac{1}{S_{g,\mathrm{max}}} \tag{6}$$

$$S_{gt} = \frac{S_{g,\mathrm{hys}}}{1 + C\, S_{g,\mathrm{hys}}} \tag{7}$$

with $S_{g,\mathrm{max}} = 1 - S_{wi}$. The Carlson (1981) shifted-drainage construction generates the scanning curves that connect the bounding drainage and imbibition branches during reversals.

Case M five types span the lithofacies contrast of a fluvial-channelized system while leaving each type enough cells for training at 25 × 25 × 5 resolution, and the PUNQ-S3 model of Juanes et al. (2006) is the closest published analogue. The resulting Land coefficient spread of 0.41 to 7.14 is the widest trapping contrast this grid resolves. Entry pressure is not assigned arbitrarily but coupled to rock quality through the Leverett J-function of Eq. 8 (Leverett, 1940),

$$P_{e,i} = P_{e,\mathrm{RT1}} \sqrt{\frac{\phi_i / k_i}{(\phi/k)_{\mathrm{RT1}}}} \tag{8}$$

An anchor entry pressure of 8.0 kPa is set for the highest-quality channel sand (RT1). Applying the Leverett scaling to tighter lithologies steps the entry pressures upward and produces the consistent ladder from 8.0 kPa (RT1) to 42.8 kPa (RT5) in Table 2. A low Land coefficient corresponds to a high trapped fraction, so the shale RT5 (C = 0.41) strands the largest residual saturation and the channel sand RT1 (C = 7.14) the smallest. The HYSKRG column of Table 2 reports the maximum residual gas saturation $S_{gr,max}$, not the Land coefficient (C).

2.4 Hysteresis classification

CMG-GEM tracks the saturation history of each cell internally, because the Land and Carlson constructions require the historical maximum gas saturation, but it does not export the resulting hysteretic state as an output array; only the saturation fields and the trapped-gas saturation are reported. A rule-based classifier is therefore applied to the simulated water-saturation trajectory of each cell, assigning one of five categorical labels at every report step from the sign and the persistence of the saturation change. Class 0 is the initial water-saturated state (brine). Class 1 is primary drainage, the first CO_2 invasion during injection. Class 2 is first imbibition, brine re-invasion after shut-in. Class 3 is second drainage, CO_2 re-entry during buoyant migration. Class 4 is the subsequent second imbibition. A water-saturation increment threshold of 10^{-4} separates drainage from imbibition reversals. The value lies below the smallest single-step saturation change observed in the slow part of the monitoring period and above the solver convergence tolerance, so it detects genuine reversals without responding to numerical noise; its sensitivity was not tested. Predicting these labels together with the saturation fields allows the surrogate to report not only where CO_2 is located but also whether the local flow state is draining or imbibing.

2.5 Model input and output channels

An input channel in this context is one gridded field supplied to the network. Each channel is defined on the same cells as the simulation grid, and the channels are stacked into a single multivariate array so that porosity forms one channel, log-permeability a second, and so on. The neural operator learns on extracted 2D slices, either vertical 25 × 5 cross-sections or horizontal 25 × 25 layers. Slicing isolates path-dependent hysteresis learning without the memory overhead of 3D spectral convolution. Case F uses five continuous channels: porosity, log-permeability, an injector indicator, the vertical anisotropy ratio kv/kh, and a normalized timestep. The 3D slices append a layer index, giving six channels for Case D. Case M adds a categorical rock-type field of integers 1 to 5, giving seven. The models output three fields: gas saturation, water saturation, and the five-class hysteresis state. Saturation fields are predicted via continuous regression, while the

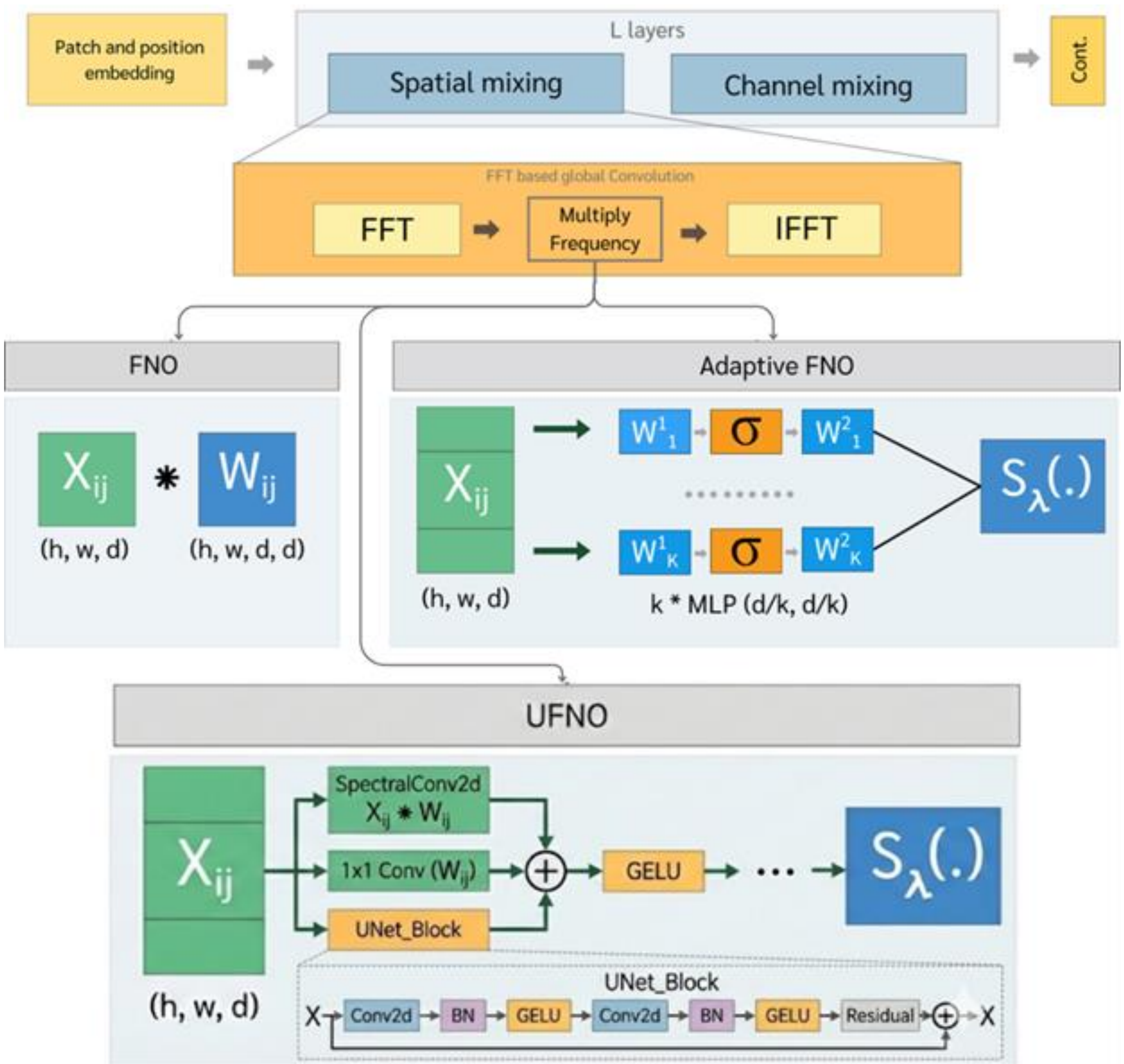

Figure 3: Neural operator architectures. Top: the shared Fourier-transform-based global convolution, with spatial mixing and channel mixing. Middle left: FNO spectral convolution with a learnable complex weight tensor. Middle right: AFNO, which applies a soft threshold in the Fourier domain and retains only the strongest modes. Bottom: U-FNO, which adds a U-Net encoder-decoder branch in parallel with the spectral path.

hysteresis state is predicted via discrete classification. The five-class hysteresis field is read from a single categorical map instead of being inferred by comparing two saturation fields cell by cell. Predicting it jointly with the saturations ties the classification to the saturation dynamics and keeps the shared representation consistent (Doughty, 2007). The reservoir pressure field is excluded as a target because its behavior differs from the hyperbolic saturation fields, and treating it properly would require a study of injectivity or geomechanics.

2.6 Neural operator models

All three architectures share a common operator structure (Figure 3). The input function is lifted to a higher-dimensional representation, passed through several operator layers, and projected back to the output (Li et al., 2021; Kovachki et al., 2023). Each operator layer mixes information in two ways. A global path takes the Fourier transform of the feature field, keeps the low-frequency modes, multiplies them by learnable weights, and transforms back, which propagates large-scale effects such as pressure diffusion and buoyancy across the whole domain in one step. A local path applies an ordinary convolution, which captures sharp fronts and lithological contacts. The three architectures differ in how they balance these paths. The FNO uses the global Fourier path with a simple local convolution (Li et al., 2021). The AFNO applies a soft threshold in the Fourier domain that retains only the strongest modes and discards the remainder, which suits globally smooth fields (Guibas et al., 2022). The U-FNO adds a U-Net branch to the local path, which strengthens its handling of sharp boundaries (Wen, Li, Azizzadenesheli, et al., 2022). The trade-off across them is therefore between global spectral reach and local boundary detail, which is the relevant axis for a flow problem that couples basin-scale migration to facies-scale trapping (Li et al., 2021; Kovachki et al., 2023).

The FNO update for layer l is given by Eq. 9,

$$v_{l+1}(x) = \sigma\left(W\, v_l(x) + \mathcal{F}^{-1}\left(R_\phi \,.\, \mathcal{F}(v_l)\right)(x)\right) \qquad (9)$$

where $\mathscr{F}$ denotes the fast Fourier transform, $R\phi$ is a learnable complex weight tensor that mixes high-order modes to capture global flow physics, W is a linear residual connection (implemented as a 1×1 convolution), and σ is the GELU activation function. By operating in the frequency domain, FNO efficiently captures global pressure diffusion and buoyancy-driven flow. The U-FNO update sums three branches, as given by Eq. 10,

$$v_{l+1}(x) = \sigma\left(\kappa_{spec}\,(v_l) + W\,(v_l) + U_{net}\,(v_l)\right) \qquad (10)$$

where K_{spec} is the spectral convolution (global), W is a 1×1 convolution (linear residual), and U_{net} is a convolutional encoder–decoder with batch normalization and skip connections (local). This architecture preserves sharp saturation gradients at lithological boundaries while maintaining global plume dynamics.

The comparison in this study is between neural operators. The three architectures all share the spectral layer of Eq. 9 and differ only in how they combine it with a local path. Convolutional and graph-based surrogates are excluded, because the question is which operator inductive bias resolves spatially varying trapping, and that operator versus convolution comparison already exists for non-hysteretic problems (Wen et al., 2022; Mao et al., 2025). The consequence is that these results bound spectral operators and do not speak to convolutional baselines. For the 25×25 grid we keep 12×12 Fourier modes, and for the 25×5 grid we keep 12×2 modes to respect the Nyquist limit of the five-cell dimension.

2.7 Loss function and training

The models are trained using a composite objective function consisting of mean-squared error (MSE) for both gas and water saturation, and cross-entropy loss for hysteresis classification. The regression terms are given full weight (1.0), while the classification loss is weighted by 0.5 to balance accurate saturation prediction with state identification (Eq. 11).

$$\mathcal{L} = \mathrm{MSE}(S_g) + \mathrm{MSE}(S_w) + 0.5\,\mathrm{CE}(h) \tag{11}$$

Three spectral architectures are evaluated: FNO, U-FNO and AFNO. Parameter counts are matched across architectures within each case, so performance differences reflect inductive biases rather than capacity. Models train with AdamW at an initial learning rate of 10^{-3}, halved every 20 epochs. Complete geological realizations are held out for testing, which evaluates generalization to unseen geology. Three temporal scenarios are trained separately: injection (days 0–9132, the 25-year injection window), post-injection (days 9497–54787, the shut-in monitoring period during which no well operates), and both (the full 0–54787-day cycle). Day 9132 is the last report step before shut-in and day 9497 the first after it, so the two windows are contiguous and the apparent 365-day gap is only the annual reporting interval. For Cases D and M, 72 of the 90 realizations are used for training and 18 for testing; Case F uses a 40/10 split of its 50 realizations.

2.8 Grid refinement and evaluation

Grid refinement is assessed by refining the 3D geologies laterally from 25 × 25 × 5 to 44 × 44 × 5 while preserving the areal extent, then evaluating a coarse-grid model on the refined grid. The refinement acts in the two lateral directions only. The five-layer vertical dimension is unchanged, so a vertical slice goes from 25 × 5 to 44 × 5 and the vertical mode budget of two is

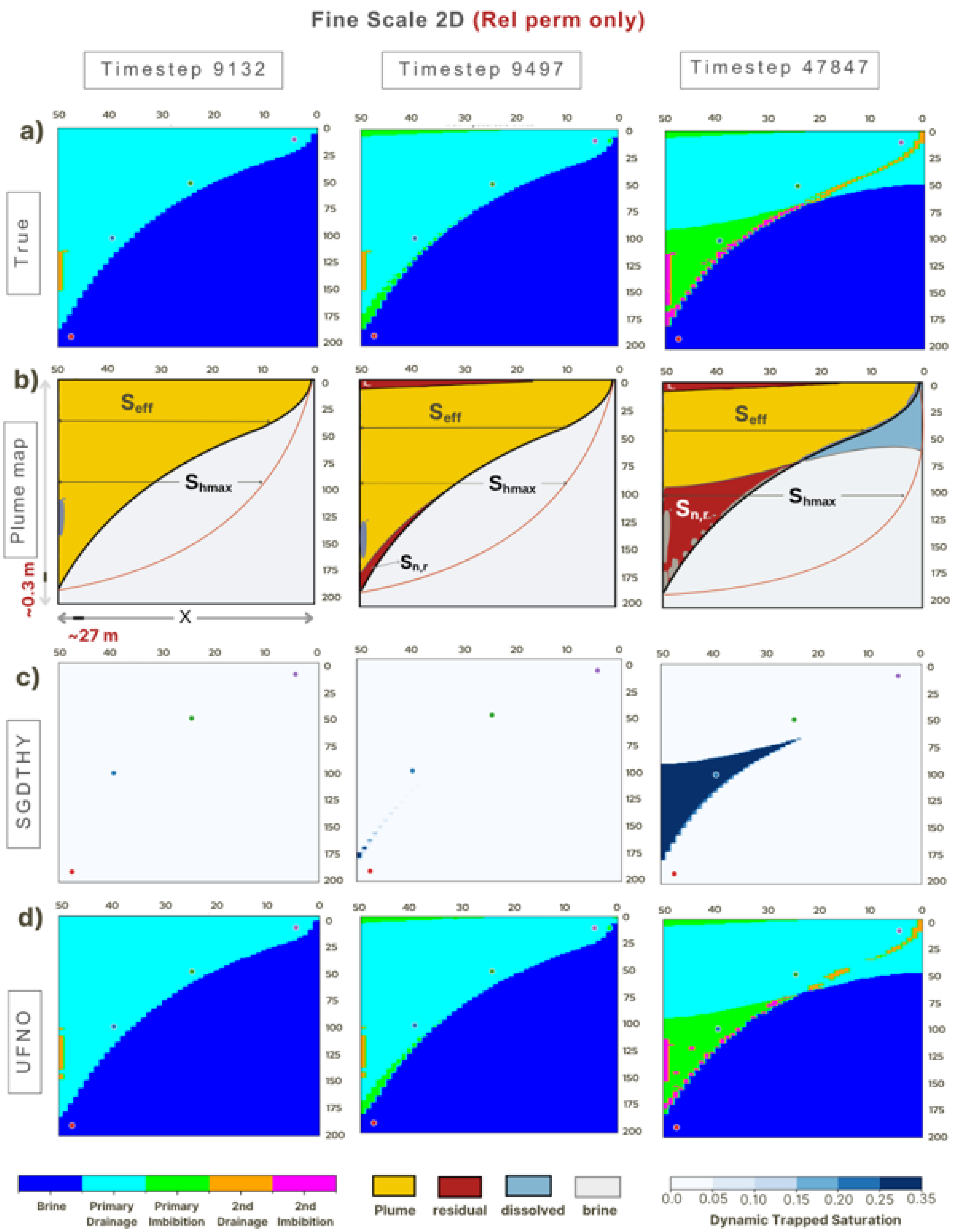

Figure 4: Case F relative permeability hysteresis results at three report steps (9132, 9497 and 47 847 days). (a) True CMG-GEM hysteresis state. (b) Plume decomposition into effective saturation, historical maximum saturation, residual, dissolved and brine zones. (c) Trapped gas saturation (SGDTHY). (d) U-FNO prediction. The report steps at 9137 and 9437 days were unseen during training.

fixed by the Nyquist limit of five cells on both grids. The test therefore probes lateral discretization invariance and not refinement across layers. Model performance on the held-out test realizations is evaluated with the coefficient of determination (R^2), the mean absolute error (MAE) and the root-mean-squared error (RMSE) for the saturations, and with categorical accuracy for the five-class hysteresis state.

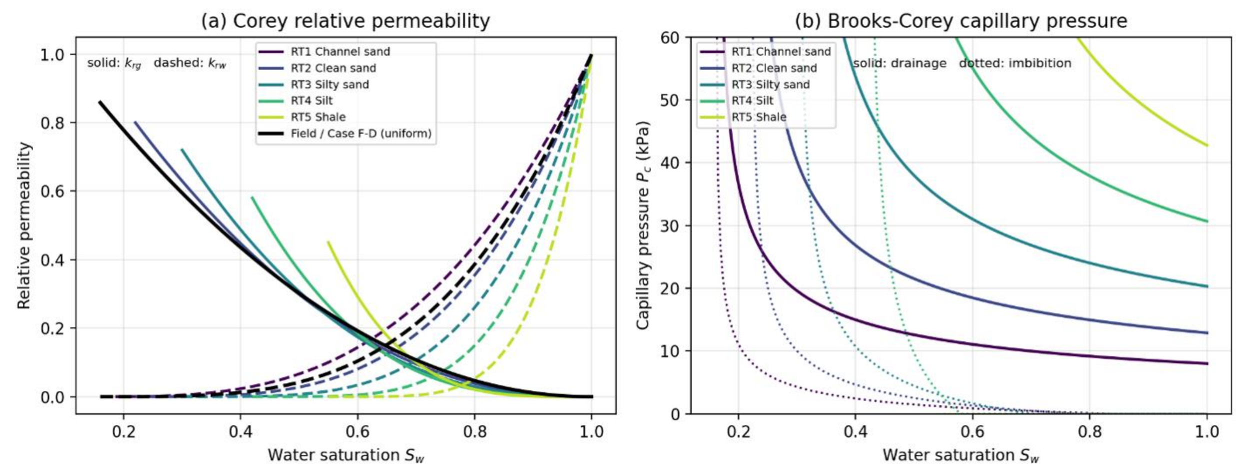

Figure 5: Constitutive relations for the uniform Case F and Case D rock type and the five Case M rock types RT1–RT5. (a) Corey relative permeability of water (krw) and gas (krg) against water saturation. (b) Brooks-Corey capillary pressure in kPa, drainage and imbibition branches, showing the Leverett-scaled entry-pressure ladder from 8.0 kPa (RT1) to 42.8 kPa (RT5). Maximum residual gas saturation ranges from 0.12 (RT1, channel sand) to 0.38 (RT5, shale).

3. Results

3.1 Uniform trapping

Under uniform trapping, all three architectures reproduced the saturation and hysteresis fields accurately (Table 3). Case F reached a gas-saturation R^2 of 0.983 to 0.996 with hysteresis classification accuracy of 98.4 to 98.7%, and Case D reached R^2 of 0.994 to 0.9999 with hysteresis accuracy above 99.8% (Figures 4 and 6). The Case D result held under both the relative-permeability (RP) and the relative permeability with capillary pressure (RPC) settings, so adding a second history-dependent constitutive relation did not by itself reduce accuracy while the trapping law remained spatially uniform.

At field scale the standard FNO matched the larger U-FNO using fewer parameters, which indicates that the U-Net branch contributes little when the saturation pattern is spatially regular

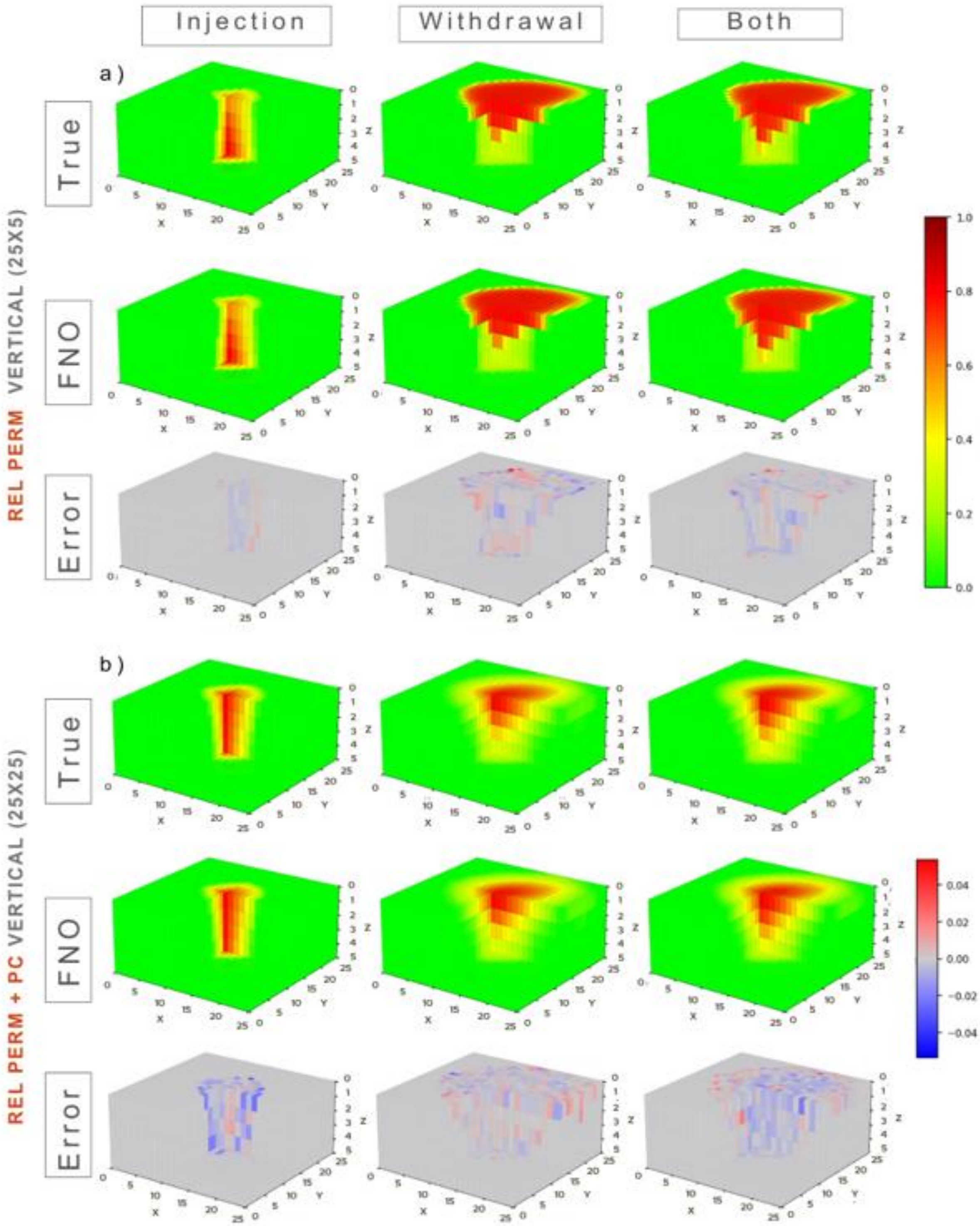

Figure 6: Case D results. (a) Relative permeability hysteresis (RP), vertical orientation, 25 × 5 cells. (b) Relative permeability with capillary pressure hysteresis (RPC), horizontal orientation, 25 × 25 cells. Each block covers the injection, post-injection and combined scenarios and shows the true field, the FNO prediction and the signed error. The error range of ±0.05 indicates near-complete reconstruction under uniform trapping.

(Figure 7). For reference, Wen et al. (2022) reported $R^2 = 0.981$ for a non-hysteretic surrogate on a comparable problem, so the uniform-trapping models here achieve equal or higher accuracy while additionally predicting the hysteresis state. These R^2 values are computed over every cell, including cells the plume never reaches, so part of the score reflects correct prediction of the gas-free background (Section 2.8). A single trapping law is therefore within the representational capacity of all three architectures, and the discriminating test is lithofacies heterogeneity.

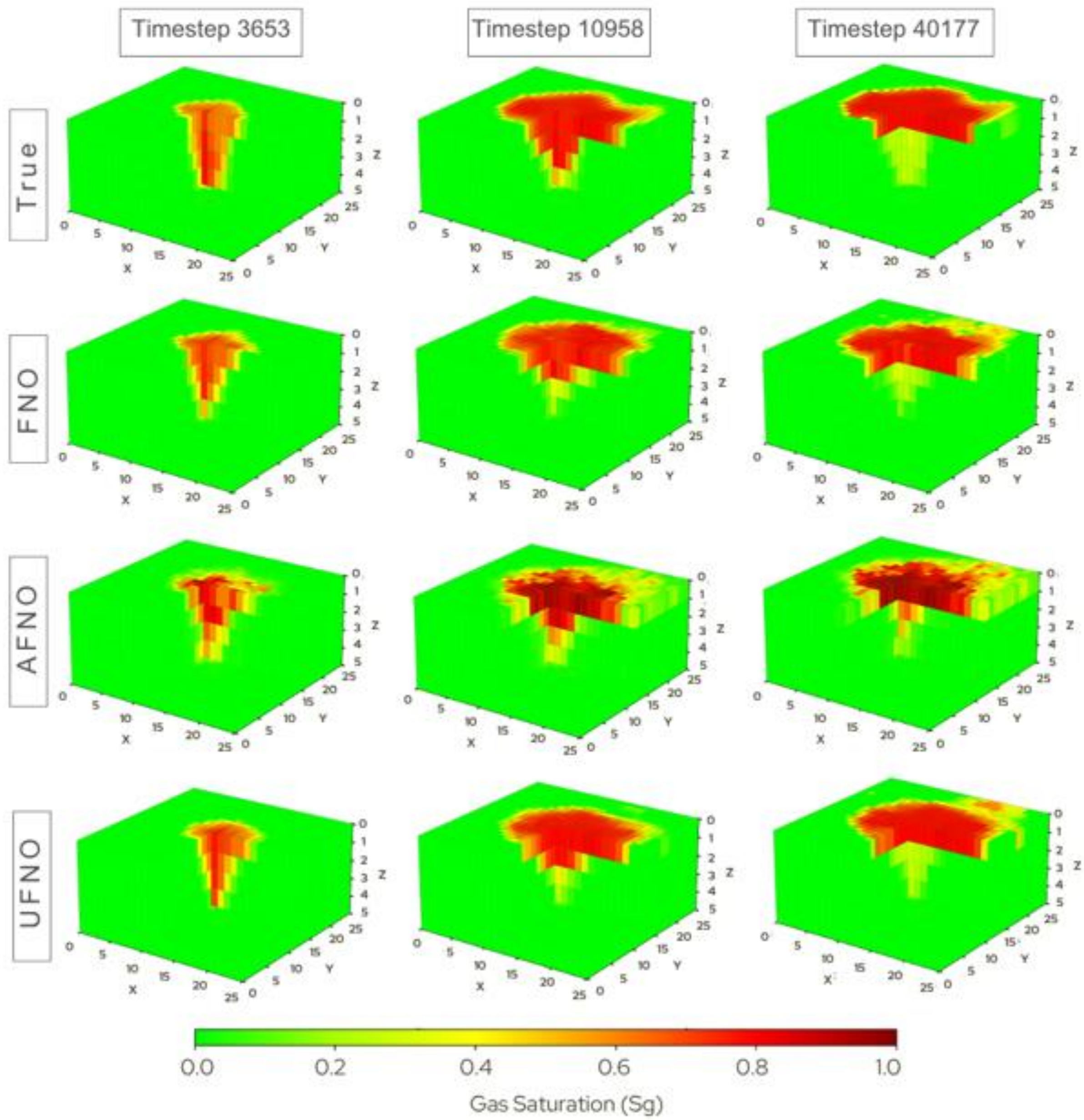

Figure 7: Case D architecture comparison for gas saturation at three report steps (3653, 10 958 and 40 177 days). Rows: true CMG-GEM field, FNO, AFNO and U-FNO. The FNO and U-FNO track the front geometry closely, whereas the AFNO smooths it, which is consistent with its purely spectral processing.

Table 3: Model performance summary for the combined injection and post-injection scenario, across all cases, slice orientations and architectures. Metrics are the hysteresis classification accuracy, the gas saturation R^2, the mean absolute error (MAE), the root-mean-squared error (RMSE) and the inference time per slice.

Scale	Input channels	Hysteresis complexity	Orientation	Model	Hys acc	Gas R2	Gas MAE (e4)	Gas RMSE (e4)	Inference time (s)
Case F	5-ch	RP	vertical	AFNO	98.41	0.9825	150.43	480.04	0.02036
				FNO	98.38	0.9915	55.4	334.31	0.03036
				UFNO	98.69	0.9956	38.38	241.74	0.08545
Case D	6-ch	RP	horizontal	AFNO	99.92	0.9985	21.27	71.01	0.00185
				FNO	99.95	0.9999	5.3	18.32	0.00216
				UFNO	99.95	0.9999	3.88	14.94	0.00469
			vertical	AFNO	99.95	0.9983	26.5	76.17	0.0004
				FNO	99.96	0.9998	7.84	23.53	0.00045
				UFNO	99.96	0.9997	10.97	32.68	0.00102
		RPC	horizontal	AFNO	99.9	0.9979	23.07	67.94	0.00185
				FNO	99.93	0.9996	10.39	29.03	0.00216
				UFNO	99.93	0.9996	12.31	30.46	0.00469
			vertical	AFNO	99.87	0.9939	48.01	115.67	0.0004
				FNO	99.94	0.9994	14.11	36.14	0.00045
				UFNO	99.9	0.9988	21.19	51.42	0.00102
Case M	6-ch	RP	horizontal	AFNO	93.38	0.761	296.89	905.54	0.00185
				FNO	94.75	0.8628	184.4	686.06	0.00216
				UFNO	94.94	0.8769	170.49	650.05	0.00469
			vertical	AFNO	94.67	0.8364	249.37	749.27	0.0004
				FNO	95	0.8648	171.71	681.08	0.00045
				UFNO	95.31	0.8823	155.04	635.4	0.00102
		RPC	horizontal	AFNO	80.96	0.5469	309.79	696.93	0.00185
				FNO	82.06	0.6552	242.92	607.98	0.00216
				UFNO	82.92	0.6895	228.54	576.93	0.00469
			vertical	AFNO	83.74	0.701	240.61	566.12	0.0004
				FNO	82.65	0.6909	212.05	575.57	0.00045
				UFNO	82.35	0.6845	213.53	581.55	0.00102
	7-ch	RP	vertical	AFNO	99.64	0.9956	13	44.22	0.0004
				FNO	99.89	0.9996	10.4	38.45	0.0008
				UFNO	99.97	0.9999	9.15	35.37	0.001
			hor izo nta	AFNO	99.19	0.9942	13	41.41	0.0018

		FNO	99.44	0.9982	10.4	36.01	0.0022
		UFNO	99.52	0.9985	9.15	33.13	0.0047
RPC	vertical	AFNO	99.36	0.9857	63.98	130.87	0.0004
		FNO	99.61	0.9897	51.18	113.8	0.0008
		UFNO	99.69	0.99	45.04	104.7	0.001
	horizontal	AFNO	99.29	0.9919	41.42	82.83	0.0018
		FNO	99.54	0.9959	33.14	72.03	0.0022
		UFNO	99.62	0.9962	29.16	66.27	0.0047

3.2 Rock-type heterogeneity

Introducing spatially varying trapping laws reduced accuracy substantially when only continuous input channels were supplied. Case M assigns five rock types with maximum residual gas saturation ranging from 0.12 to 0.38. With six continuous channels, gas-saturation R^2 fell to 0.76 to 0.88 under the RP setting and to 0.55 to 0.70 under the RPC setting, while hysteresis classification accuracy fell to 93.4 to 95.3% and to 81.0 to 83.7% respectively (Table 3). The error no longer concentrated at the plume front but extended through the interior of the domain, including cells beneath the plume (Figure 8).

The six-channel input does not contain the lithofacies boundaries in a form the operator can use. Rock type is assigned from porosity and permeability by fixed thresholds (Section 2.1), so a six-channel network must reconstruct a piecewise-constant field, and the step change in maximum residual gas saturation that follows from it, out of two smooth fields. A step function carries energy at every wavenumber, whereas the spectral layer retains only twelve lateral modes (Section 2.6), so the target is not representable within the available mode budget. The RP setting requires one such reconstruction and the RPC setting requires a second, which accounts for the lower accuracy when capillary pressure hysteresis is also active. The U-FNO was the strongest of the three architectures in this configuration but did not close the gap, which locates the limitation in the inputs rather than in network capacity.

3.3 The rock-type input channel

Supplying rock type as a seventh, categorical channel returned accuracy to the uniform-trapping level. Gas-saturation R^2 recovered to 0.994 to 0.9999 under the RP setting and to 0.986 to 0.996 under the RPC setting, and hysteresis classification accuracy returned to 99.2% or above in both (Table 3). The signed saturation error contracted to approximately ±0.08, about two orders of magnitude smaller than in the six-channel case (Figures 9 and 10).

The classification maps identify where the recovery occurs (Figure 11). Six-channel misclassification concentrates along the rock-type contacts, which are the boundaries the network had to reconstruct, whereas seven-channel misclassification is low in amplitude and shows no boundary structure. Supplying the discontinuity as an explicit field removes the requirement to synthesize it, and the local trapping coefficient follows from it. The recovered models also reproduce the trapped-gas accumulation in Cases D and M (Figure 12). These runs used the standard FNO, because once the discontinuity is supplied the U-FNO advantage observed at six channels disappears. The categorical channel adds no geological information, since rock type is already determined by porosity and permeability; what it adds is a representation the spectral operator can carry directly. It is, however, a broadband field, and Section 3.6 shows that this places the grid-transfer property of the operator at risk.

3.4 Comparison across the three neural operator architectures

Figure 13 compares the three architectures across the cases. Every configuration was trained once under a single random seed, so all values are point estimates without a variance estimate, and differences of one or two hundredths in R^2 are not a reliable ordering. Three patterns are larger than that uncertainty. First, in Case F and in uniform Case D the three architectures fall within about one percentage point of one another, and the FNO and U-FNO are equivalent for practical purposes. Second, in six-channel Case M the U-FNO leads three of the four configurations and the AFNO trails by up to 0.14 in R^2, an order of magnitude larger than the difference between the FNO and the U-FNO. The AFNO trails for the same spectral reason that six channels fail: its soft threshold discards the weaker Fourier modes, so it is the least able of the three to represent a step-function target. Third, once rock type is supplied at seven channels the discontinuity no longer has to be reconstructed and the standard FNO reaches the same accuracy on its own. Architecture choice therefore matters less than input completeness. The FNO and U-FNO are interchangeable when the inputs resolve the lithofacies, the U-FNO retains a modest advantage when the network must infer heterogeneity from continuous fields, and the AFNO is the weakest of the three for this problem.

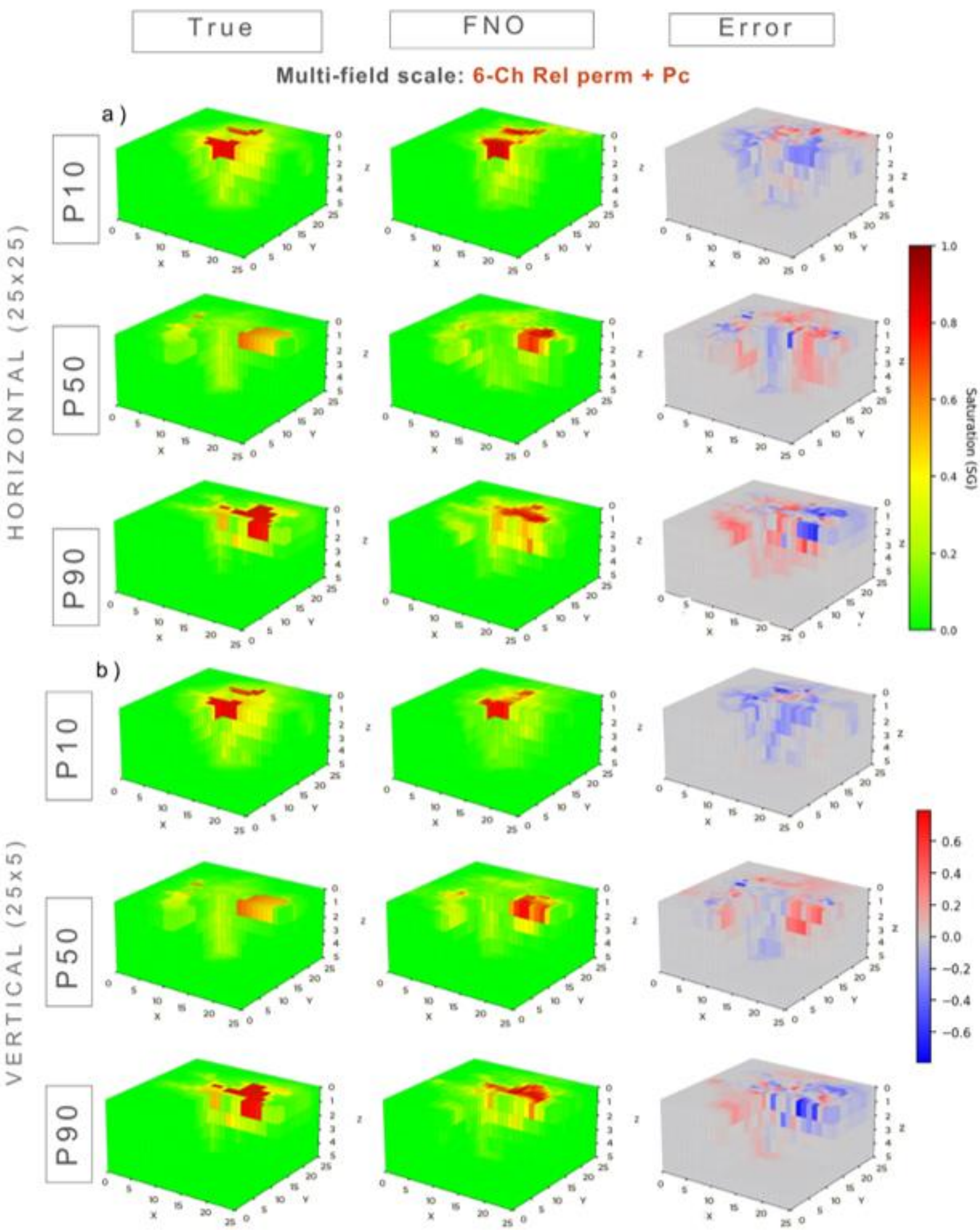

Figure 8: Case M six-channel results under relative permeability with capillary pressure hysteresis (RPC). (a) Horizontal orientation, 25 × 25 cells. (b) Vertical orientation, 25 × 5 cells, for the P10, P50 and P90 realizations. Each block shows the true field, the FNO prediction and the signed error. Structured errors within and beneath the plume show that six continuous channels do not resolve spatially varying trapping.

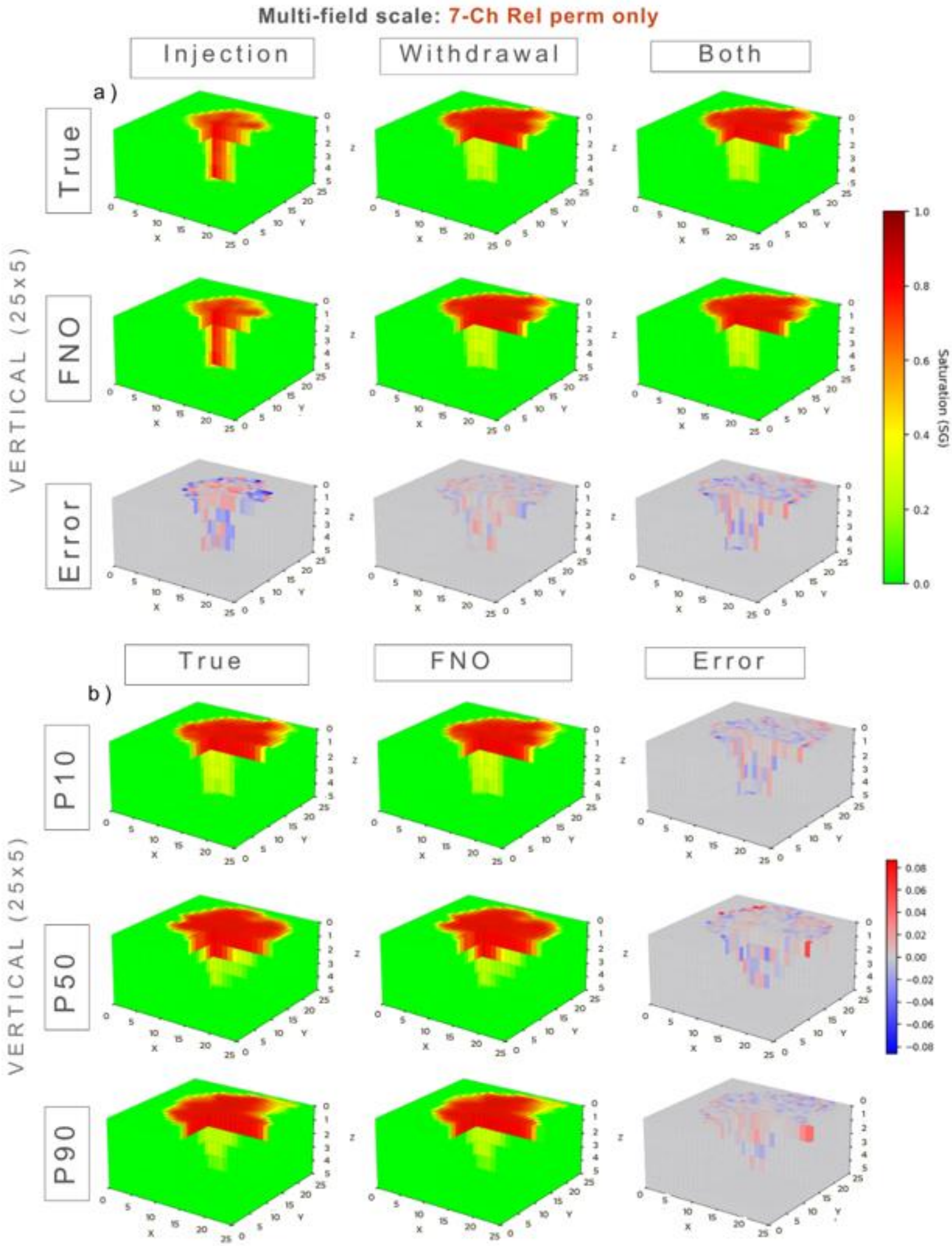

Figure 9: Case M seven-channel results under relative permeability hysteresis (RP), vertical orientation, 25 × 5 cells. (a) Injection, post-injection and combined scenarios, showing the true field, the FNO prediction and the signed error. (b) The P10, P50 and P90 realizations. The signed-error range of ±0.08 recovers the uniform-trapping accuracy.

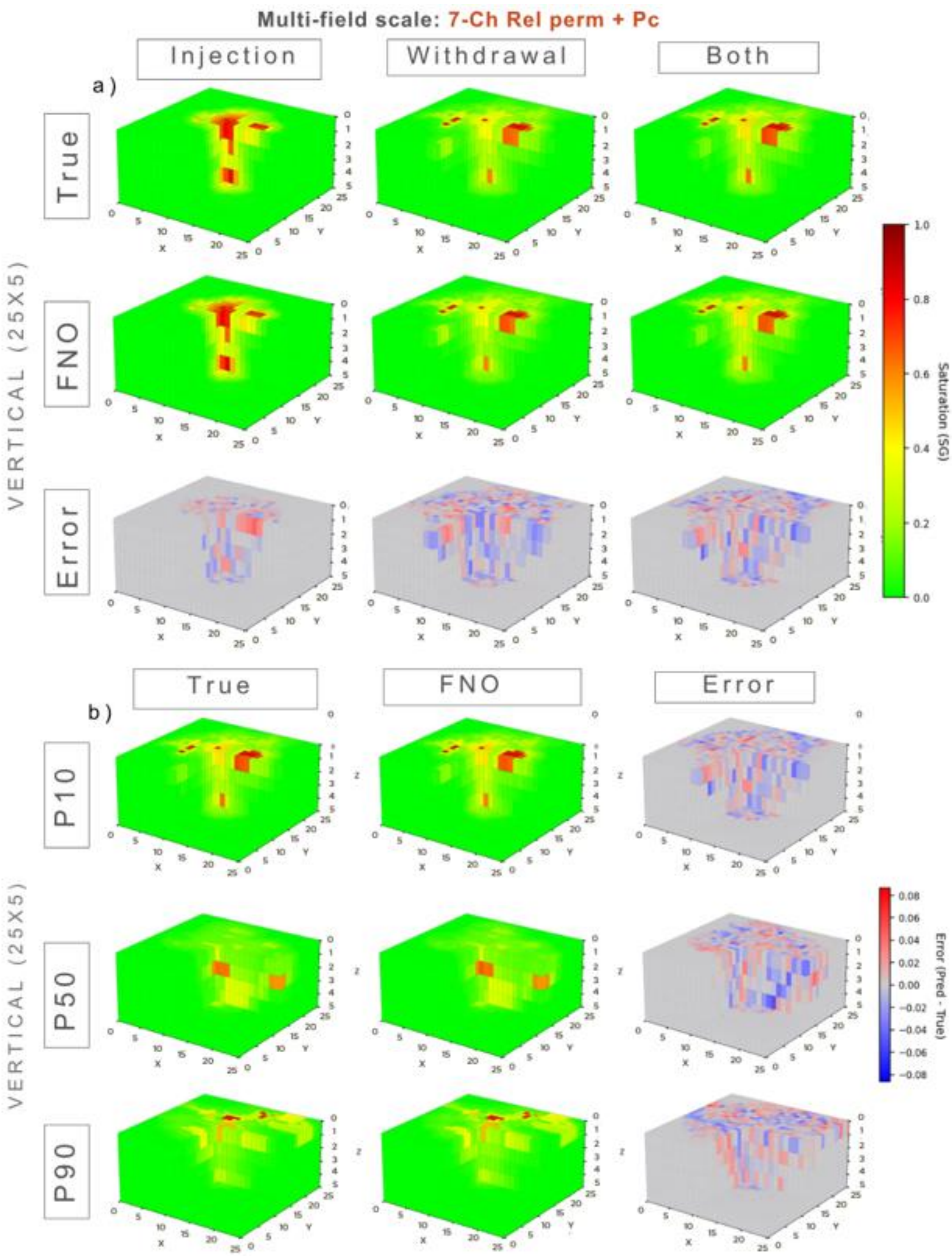

Figure 10: Case M seven-channel results under relative permeability with capillary pressure hysteresis (RPC), vertical orientation, 25 × 5 cells. The layout follows Figure 9. Accuracy is recovered in the more demanding physics setting once rock type is supplied explicitly.

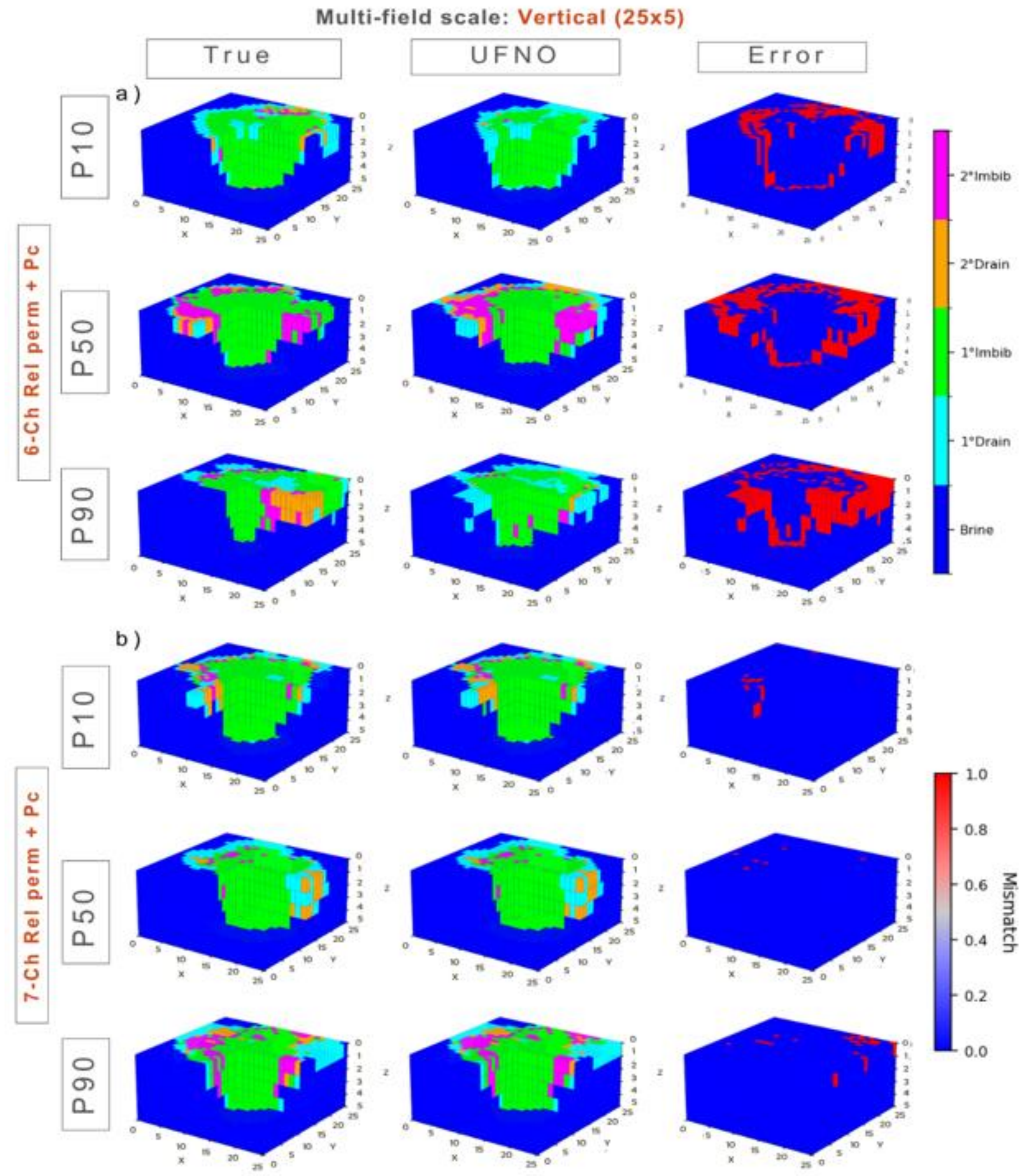

Figure 11: Hysteresis-state classification under relative permeability with capillary pressure hysteresis (RPC), vertical orientation. (a) Six-channel model. (b) Seven-channel model. Each shows the true state, the U-FNO prediction and the mismatch map for the P10, P50 and P90 realizations. Classes are brine, primary drainage, first imbibition, second drainage and second imbibition. Six-channel mismatch concentrates at rock-type contacts; seven-channel mismatch shows no boundary structure.

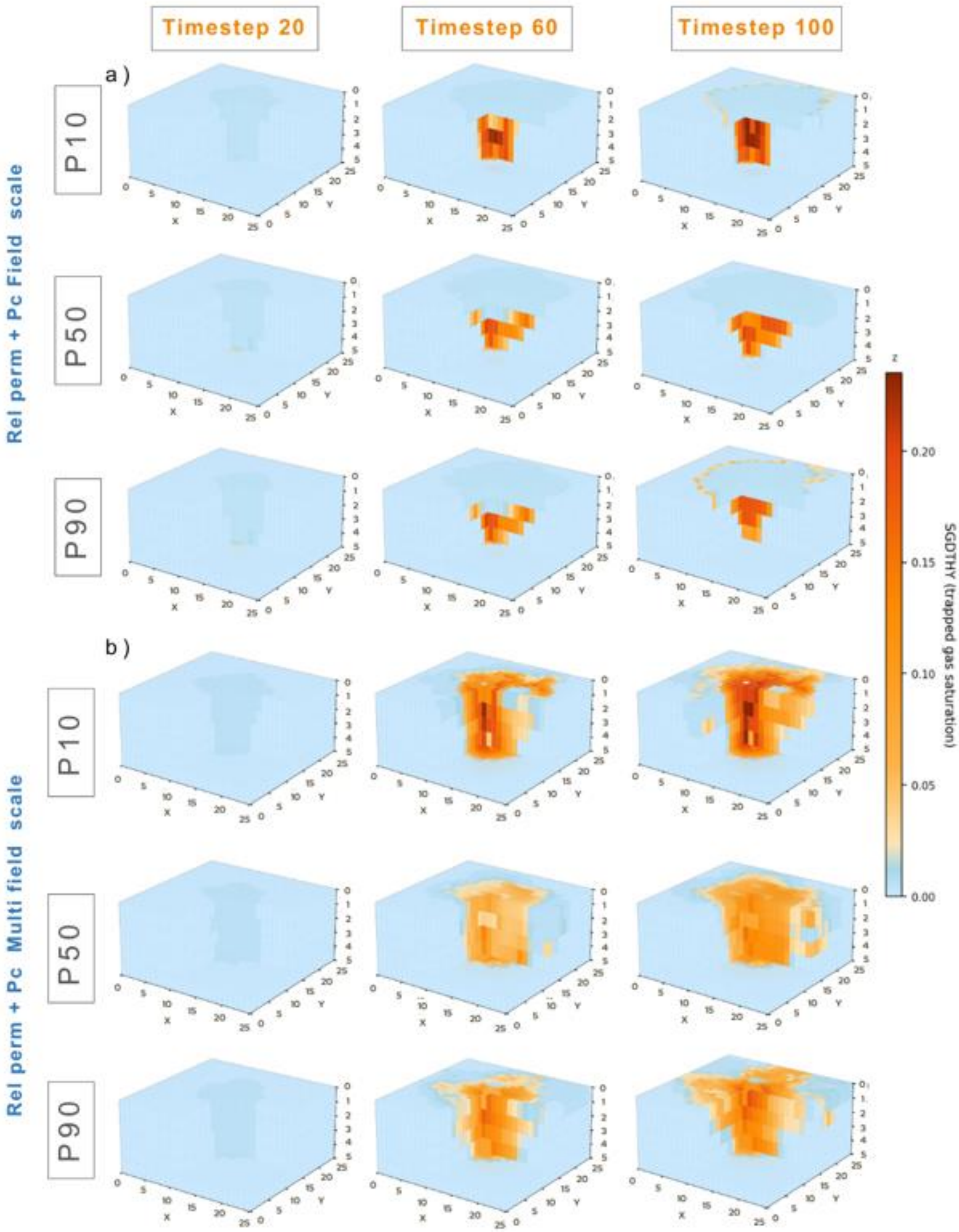

Figure 12: Trapped gas saturation (SGDTHY) at report steps 20, 60 and 100. (a) Case D under relative permeability with capillary pressure hysteresis. (b) Case M under the same setting, for the P10, P50 and P90 realizations. The recovered models reproduce the spatial pattern and the magnitude of residual trapping.

3.5 Computational speed-up

Inference costs approximately 1ms per two-dimensional slice on a single NVIDIA A40 GPU. A full realization comprises 161 report steps across 25 vertical slices, or 4025 slice evaluations, and is therefore reconstructed in approximately 4s, against hours per realization for the equivalent CMG-GEM run. The resulting speed-up is three to four orders of magnitude, which is sufficient to make Monte Carlo uncertainty quantification, history matching and injection optimization practical at ensemble scale.

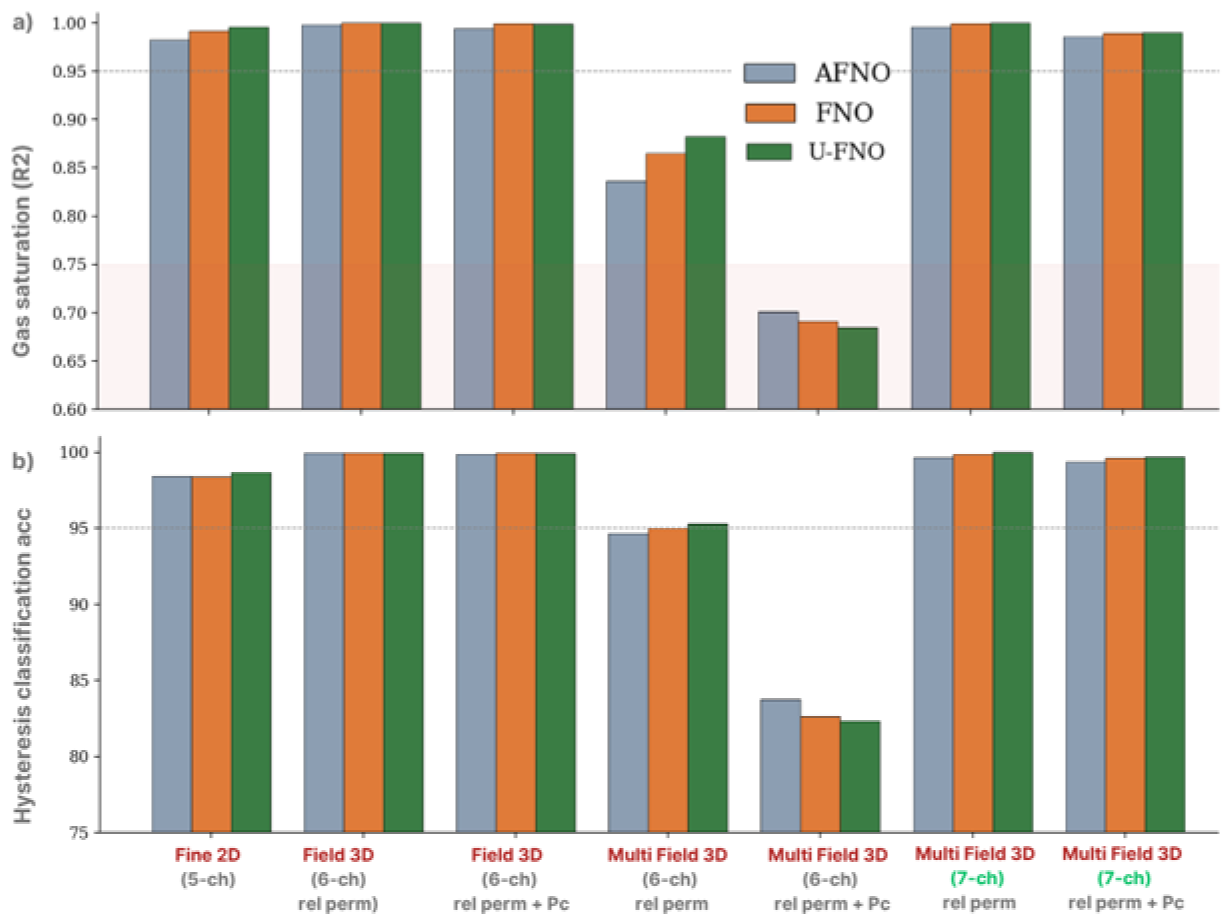

Figure 13: Comparison of the three architectures across the case hierarchy, combined scenario. (a) Gas saturation accuracy. (b) Hysteresis classification accuracy, for AFNO, FNO and U-FNO. The panels show the uniform-trapping cases, the accuracy gap at six channels in Case M, and the recovery once rock type is supplied as the seventh channel.

Reaching a condition in which trapping could be tested required the long monitoring horizon. The first 25 years produced less than 2% trapped gas, too little to exercise the hysteresis, and the trapped fraction approached 30% only beyond 75 years. Surrogate studies of residual trapping must therefore extend well past the injection period, or they will train on a period in which the process under study is barely active.

Table 4: Lateral grid-transfer results. For each channel configuration, temporal scenario and slice geometry, the table gives the native and transferred R2 for gas and water saturation, the native and transferred hysteresis classification accuracy, and the number of evaluation samples.

Channels	Scenario	Grid	Native R^2 (Sg)	Transfer R^2 (Sg)	Native R^2 (Sw)	Transfer R^2 (Sw)	Native Hys acc	Transfer Hys acc	n samples
6-ch	injection	25x5	0.8633	0.5595	0.8598	0.5591	98.28	96.51	16200
6-ch	injection	44x5	0.839	0.4993	0.8385	0.5063	98.27	95.76	28512
6-ch	withdrawal	25x5	0.8584	0.7319	0.8584	0.7319	94.32	92.49	56250
6-ch	withdrawal	44x5	0.8646	0.6136	0.8646	0.6141	94.94	90.46	99000
6-ch	both	25x5	0.8717	0.6829	0.8717	0.6829	95.4	92.63	72450
6-ch	both	44x5	0.8482	0.5893	0.8482	0.5891	95.65	90.91	127512
7-ch	injection	25x5	0.9988	0.5155	0.9988	0.5155	99.72	95.1	13500
7-ch	injection	44x5	0.9992	0.2532	0.9992	0.2532	99.82	94.2	23760
7-ch	withdrawal	25x5	0.9996	0.5341	0.9996	0.534	99.89	91.07	33750
7-ch	withdrawal	44x5	0.9995	-0.0866	0.9995	-0.0866	99.91	86.03	59400
7-ch	both	25x5	0.9993	0.7549	0.9993	0.7549	99.86	94.21	47250
7-ch	both	44x5	0.9992	0.0338	0.9992	0.0338	99.88	88.23	83160

3.6 Grid transfer behavior

Transfer was tested on the Case M relative-permeability configuration by refining the lateral grid from 25 × 25 × 5 to 44 × 44 × 5 while preserving the areal extent, so a vertical slice changes from 25 × 5 to 44 × 5 cells (Section 2.8). A model trained at one lateral grid was then applied to the other (Table 4). The six-channel continuous model retained positive skill in both directions, with R^2 falling from 0.87 natively to 0.68 on transfer and the residual error distributed across the plume (Figure 14). The seven-channel model behaved asymmetrically. Fine-to-coarse transfer retained useful skill, with R^2 of 0.75 against a native value of 0.999, whereas coarse-to-fine transfer fell to 0.03 and, in the post-injection window, to −0.09, and the predicted plume almost disappeared (Figure 15; Table 4). Hysteresis classification accuracy remained above 86% throughout showing that cross entropy loss significance.

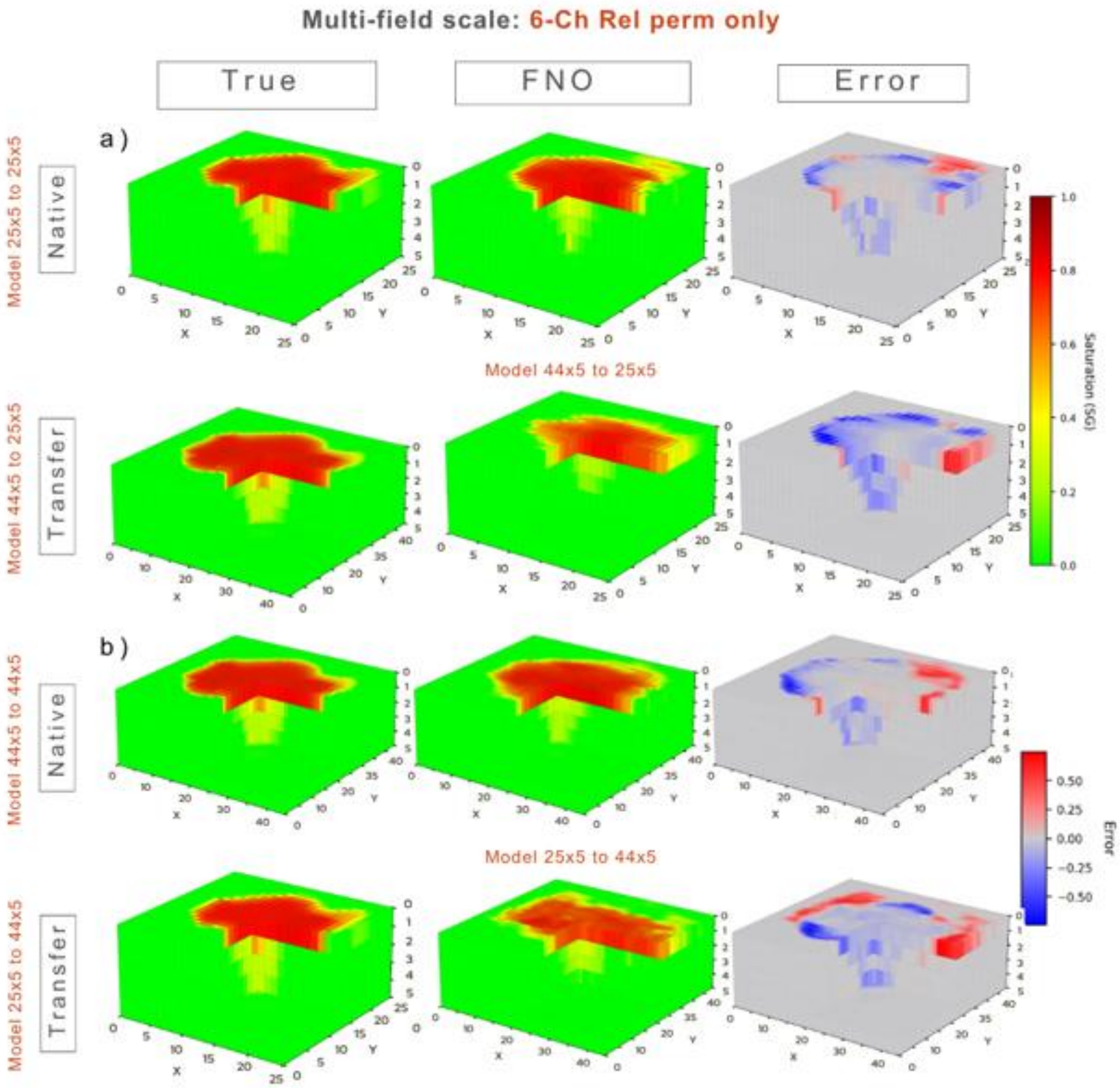

Figure 14: Six-channel relative permeability grid transfer. (a) Native 25 × 5 and transfer from 44 × 5 to 25 × 5. (b) Native 44 × 5 and transfer from 25 × 5 to 44 × 5. Columns: true field, FNO prediction, signed error. Transfer reduces accuracy in both directions but retains positive skill.

The spectral content of the input channels accounts for this asymmetry (Figure 16). A continuous channel such as porosity is smooth and band-limited, and its energy is concentrated at low wavenumbers (Figure 16a, c). The categorical rock-type channel is piecewise constant with sharp contacts, so its Fourier spectrum is broadband and carries energy up to the Nyquist limit of

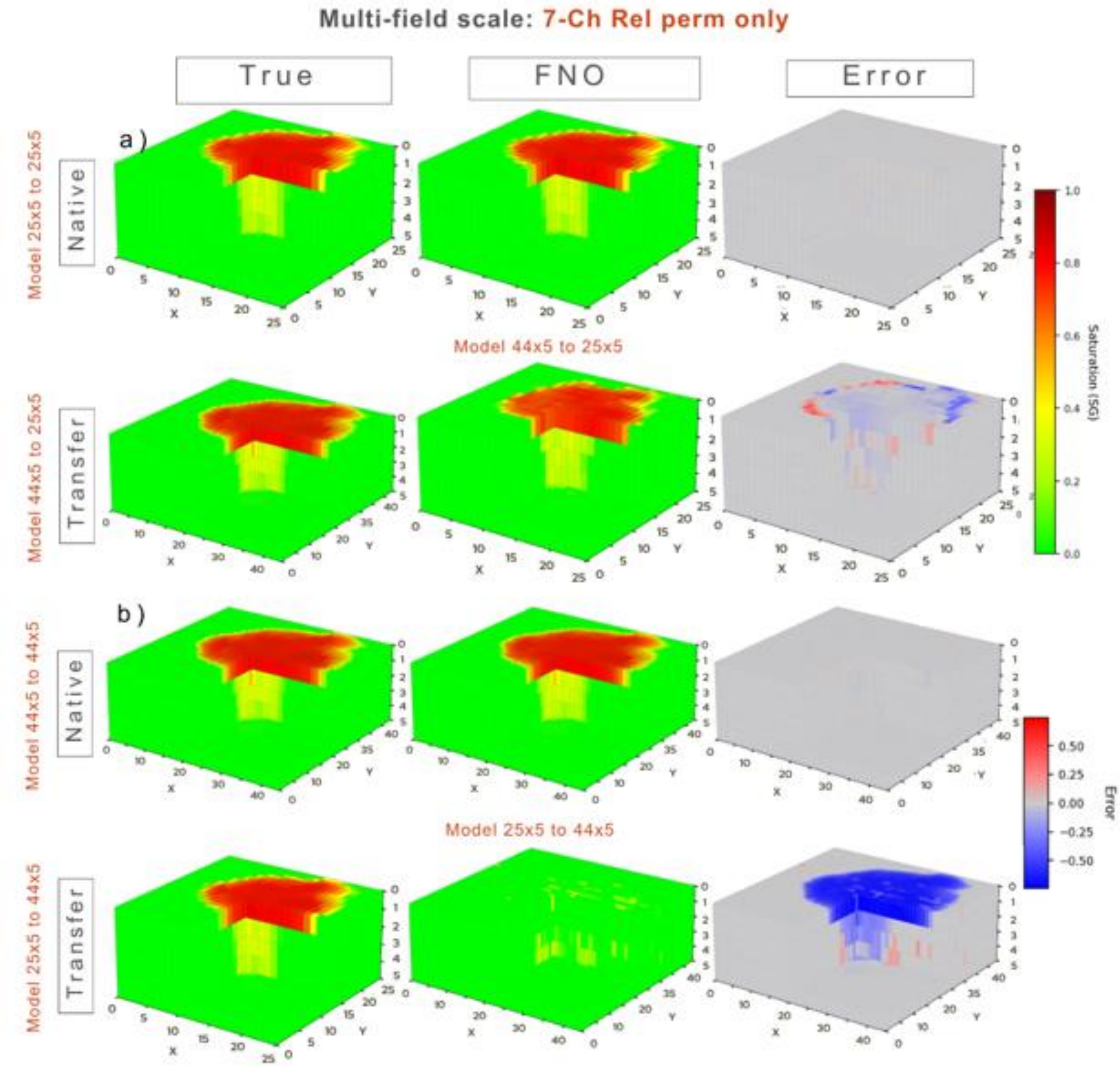

Figure 15: Seven-channel relative permeability grid transfer. (a) Native 25 × 5 and transfer from 44 × 5 to 25 × 5. (b) Native 44 × 5 and transfer from 25 × 5 to 44 × 5. Coarse-to-fine transfer fails: the predicted plume almost disappears and the signed error forms a large under-prediction block. Fine-to-coarse transfer retains useful skill.

the grid (Figure 16b, d). The operator retains a fixed set of twelve low-wavenumber modes and learns spectral weights tied to those modes at the training resolution. The continuous channels are well represented within that set and transfer without modification. The categorical channel is not, because its high-wavenumber content is a function of cell size: on a finer grid that content moves to modes for which no weights were learned, and the mapping no longer applies (Li et al., 2021; Kovachki et al., 2023). The collapse is one-sided because coarsening aggregates the categorical field by majority and preserves its low-wavenumber structure, whereas refinement requires high-wavenumber detail that the operator cannot generate. The same difficulty is familiar in reservoir modeling, where categorical lithofacies values are not preserved under grid conversion. The input that resolves lithofacies heterogeneity is therefore the input that removes the discretization invariance of the operator.

4. Discussion

4.1 Lithofacies into feature representation

The central result is that the heterogeneous accuracy gap is a limit of input representation rather than of network capacity. Rock type is a deterministic threshold function of the porosity and permeability the network already holds (Section 2.1), so the seventh channel supplies no new geological information. What it supplies is a basis. The rock type input is piecewise constant in porosity-permeability space, and a step function carries energy at every wavenumber, so a spectral layer that retains twelve lateral modes cannot synthesize it from two smooth fields. Supplying the discontinuity as an explicit field removes the requirement to synthesize it. The remedy is therefore neither a larger number of inputs nor greater capacity, but a representation the operator can carry: feature representation, not feature quantity, sets the accuracy.

The loss design supports this reading. The objective combines two MSE terms on the gas and water saturations at full weight with a cross-entropy term on the hysteresis class at half weight (Eq. 11). The half weight accelerates convergence while still training the regression and the classification together. At six channels this balanced loss did not recover the lost accuracy. Reweighting the terms did not help, and the saturation error and the hysteresis classification degraded together. The continuous and scalar inputs therefore require the additional categorical input in order to generalize.

The two saturation fields are not redundant, and predicting them jointly serves a purpose. The hysteresis labels are derived from both fields, so the dual output ties the classification to the saturation dynamics. The saturation evolution remained smooth once the hysteresis labels were included, which the pressure field would not have provided. Pressure was excluded in predictions because its behavior differs from that of the hyperbolic saturation fields. The hysteresis classes are recoverable from the saturation trajectory at each report step rather than from any explicit trapping-law formula, and this holds for both input sets and both physics settings.

The timing of the hysteresis cycles provides an independent check on the realization sampling. Across the combined scenario the starting class of each cycle varies between realizations, so the predicted and true cycle start times were compared. The model reached 96% correct hysteresis prediction on unseen report steps and reproduced the true labels closely on seen report steps of unseen realizations. This indicates that the realizations follow comparable hysteresis cycles and that the ensemble is sampled consistently across the three scenarios; a widely varying cycle start would instead indicate a poorly populated ensemble. The Case F with RP configuration illustrates the point (Figure 4). Report steps at 9137 and 9437 days fall in the injection-to-monitoring transition at years 25 and 26, both unseen during training, and were predicted with 99% accuracy.

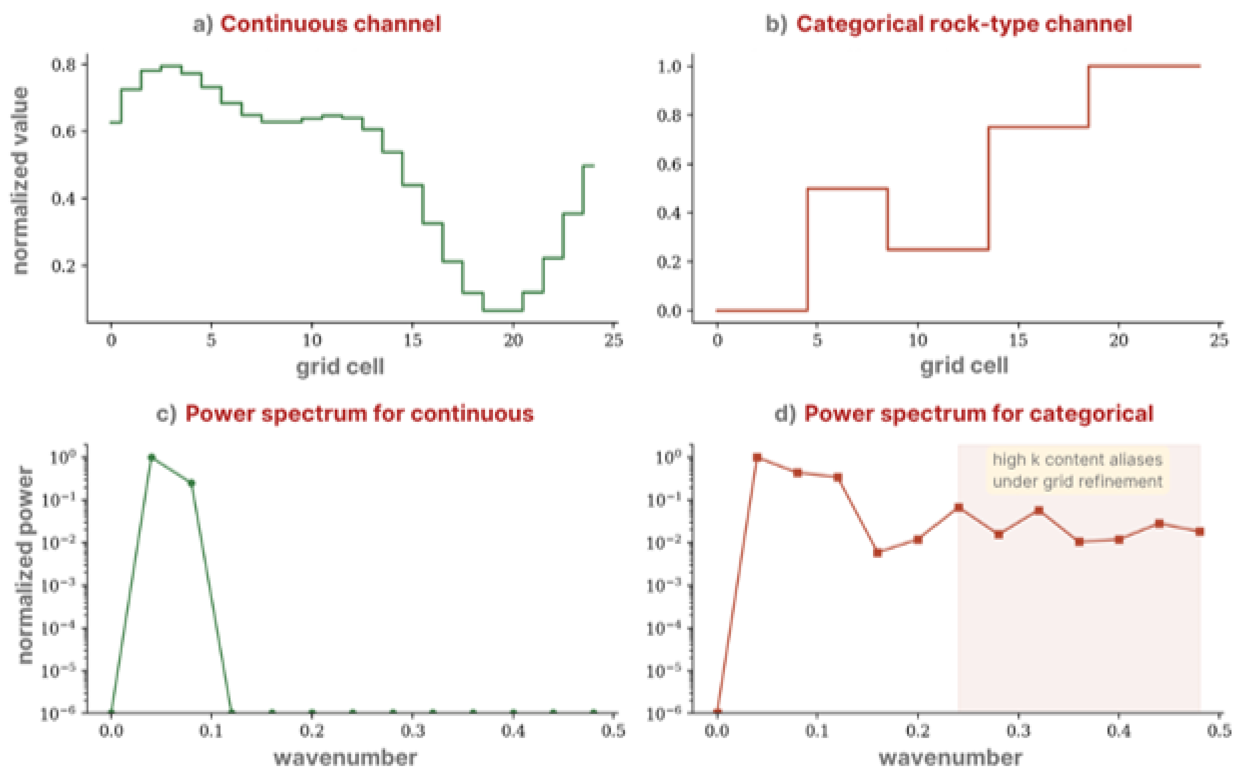

Figure 16: Spectral explanation of the grid-transfer asymmetry. (a, c) A continuous channel such as porosity is smooth and band-limited, with energy concentrated at low wavenumbers. (b, d) The categorical rock-type channel is piecewise constant, so its spectrum is broadband and carries energy to the Nyquist limit of the grid, and its high-wavenumber content shifts under refinement.

The limitation is physical rather than a failure of pattern matching. Under Case M with RP the plume shape remains close to the uniform Case D plume, yet the model does not generalize. If plume geometry alone drove the prediction, it would. The model is therefore constrained by the trapping physics behind the plume rather than by the visible pattern that conventional DL methods exploit. The contrast is clearest between the Case M with RP configuration and the corresponding RPC configuration, which produce different plume shapes from the same geology.

4.2 The categorical channel and grid transferability

The recovery described above is obtained from the one input that breaks grid transfer, which establishes a direct trade-off. The discretization invariance of a neural operator rests on an assumption: the inputs must be discretizations of band-limited functions, so that a mapping learned on a fixed set of low Fourier modes carries across grids (Li et al., 2021; Kovachki et al., 2023). The continuous channels satisfy this assumption. The categorical rock-type channel does not, because a field of sharp facies contacts holds energy at every wavenumber up to the Nyquist limit of the grid.

The six-channel transfer result requires careful interpretation. Omitting the categorical channel keeps transfer positive and bounded in both directions, which at first appears advantageous. It is not, because the six-channel model achieves only about 0.87 in R^2 on its native grid, so what transfers is a model that was inaccurate to begin with. The seven-channel model is accurate on its native grid and transfers successfully from fine to coarse resolution; only the coarse-to-fine direction fails. The relevant comparison is therefore not which model transfers, but which model is accurate enough to be worth transferring.

The seventh channel therefore purchases native accuracy by encoding exactly the broadband content that the invariance assumption excludes, so a finer grid demands high-wavenumber detail for which no spectral weights were learned. The feature that resolves lithofacies is the feature that removes invariance. Mechanically this is a spectral aliasing problem: categorical labels act as step functions and introduce sharp spatial gradients that generate high-wavenumber energy in the Fourier domain (Figure 16). One route to resolving it is to supply the trapping information without the broadband map, by replacing the discrete facies index with the corresponding Land coefficient C or maximum residual gas saturation $S_{gr,max}$ as a continuous scalar field. Such a field is band-limited by construction and would remove the artificial high-frequency contacts. Whether a smooth embedding of this kind restores accuracy while preserving transfer across resolutions has not been tested here and is the subject of ongoing work.

4.3 Comparison with previous work

FNO applications to reservoir simulation began with injection-only prediction. Wen et al. (2022) reported a gas saturation accuracy of $R^2 = 0.981$ for the U-FNO on a 2D-radial injection problem, without hysteresis, and identified post-injection hysteresis as a gap for later work. Yan et al. (2022) extended FNO surrogates to injection, withdrawal, and combined scenarios, again without hysteresis, using 2D slices of a 3D model to predict the post-injection period. These studies establish FNO capability for CO_2 flow but leave hysteresis unaddressed.

On grid transfer, Chan et al. (2026) upscaled grids through kernel computation inside the operator, but treated no hysteresis and considered upscaling alone. This study tests refinement in both directions and does so with hysteresis active. Within the CO_2 storage surrogate literature known to the authors, the Case M results are the first neural-operator treatment of spatially varying hysteresis that recovers single-rock-type accuracy, and they do so by adding the rock-type channel rather than by enlarging the network (Wen et al., 2023; Yan et al., 2022).

The constitutive treatment follows established field-scale practice. Spiteri and Juanes (2006) positioned hysteresis cycles within field-scale simulation, including the PUNQ-S3 setting, even though hysteresis is a scale-dependent process. This study adopts comparable grid spacing for the Case F, D, and M reservoir models in both the vertical and lateral directions, and maps the hysteresis classes from the two saturation fields.

4.4 Limitations and recommendations

Five limitations bound these conclusions. First, the seven-channel and transfer experiments used the FNO and the relative permeability case. The behavior of the categorical channel under the other architectures, and under capillary pressure transfer, remains to be characterized. Second, Case M and D rests on 90 realizations, which is modest for a claim about heterogeneous generalization. Third, the models operate on 2D cross-sections and neglect out-of-plane flow. Fourth, the framework predicts saturation and hysteresis but not the reservoir pressure field, which a study of injectivity or geomechanics would require. Fifth, the surrogates are deterministic and return a single point prediction for each input, with no estimate of predictive uncertainty, so the ensemble speed-up reported in Section 3.5 propagates geological uncertainty through the workflow but does not quantify the uncertainty contributed by the surrogate itself. Three routes are available and are compatible with the architecture used here: training an ensemble of operators from different seeds and reporting the spread, retaining dropout at inference to obtain an approximate posterior, and calibrating a residual model on the held-out realizations (Gal et al., 2022). The single-seed design of this study precludes all three, and any application of these surrogates to a containment-risk decision should include one of them.

Two recommendations follow. The first is to remove the invariance trade-off. Encoding the trapping properties as smooth continuous fields, in place of the categorical rock-type map, would let the six-channel input carry the lithofacies information while keeping grid transferability. The second is to use the surrogate as the forward engine of a time-lapse seismic monitoring loop. The predicted saturation and trapped-gas fields can be mapped to elastic properties through a rock-physics model and forward-modeled to a time-lapse, or 4D, seismic response, which connects the flow prediction to the seismic signal observed in the field. Embedding the surrogate inside a time-lapse full-waveform inversion (FWI) workflow would then let the saturation and permeability fields be updated directly from monitoring data in near real time (Yin et al., 2025). The accuracy and the inference speed reported here are the two properties such a monitoring loop needs, and supplying them in the heterogeneous case is the contribution this study would make toward deployable CO_2 storage surveillance.

5. Conclusions

This study evaluated three Fourier neural operator architectures, the standard FNO, the AFNO and the U-FNO, as surrogates for hysteretic CO_2–brine flow in heterogeneous saline formations. The surrogates predict the gas and brine saturation fields together with a five-class hysteresis state in a single forward pass, and were trained on hysteresis-enabled CMG-GEM simulations of a 150-year injection and monitoring cycle across three levels of geological complexity: a homogeneous fine-scale section (Case F), a field-scale model with spatially varying porosity and permeability under one trapping law (Case D), and the same field-scale model with five rock types and five trapping laws (Case M).

Explicit representation of lithofacies is necessary for accurate prediction of heterogeneous trapping. Under a uniform trapping law all three architectures reproduced the saturation and hysteresis fields accurately in both physics' settings (RP and RPC). When the trapping law varied by rock type and only continuous inputs were supplied, gas-saturation R^2 fell to 0.76–0.88 under relative permeability hysteresis (RP) and to 0.55–0.70 when capillary pressure hysteresis (RPC) was also active, and no architecture closed the gap. A key finding is that the surrogates does not follow the plume pattern blindly. The uniform (Case D with RP and RPC) and heterogeneous (Case M with RP) cases share a similar plume shape, yet the heterogeneous case fails, which shows the model is bound by the trapping physics rather than by the visible pattern that conventional deep-learning frameworks exploit. Supplying rock type as a categorical seventh channel restored R^2 to 0.986 or above and hysteresis accuracy to 99.2% or above. The input count was not the deciding factor. Feature relevance was, once the sample count was sufficient.

The same channel carries a cost in grid transfer. With seven channels, fine-to-coarse transfer retained useful skill while coarse-to-fine transfer collapsed, whereas the six-channel model transferred in both directions but from a native accuracy that was low to begin with. A single spectral band limit explains both outcomes: supplying the discontinuity removes the accuracy deficit and creates the transfer deficit. The trade-off between lithofacies sensitivity and bidirectional grid transferability is the central open problem this work identifies, and the practical consequence is that surrogates used for capacity screening, monitoring interpretation or containment-risk assessment in a multi-facies formation must encode the facies architecture explicitly.

Across the architectures, all three performed close to one another, but the AFNO struggled most, so the U-FNO and FNO are the stronger choices. Classifying the hysteresis state in the same forward pass, at half loss weight, also validated the ensemble sampling. Comparing the start of each hysteresis cycle in the prediction against the ground truth showed that the realizations balance well across the percentile ranges. These conclusions rest on 2D slices of a five-layer grid, on 90 realizations per field-scale case, and on single-seed training without an estimate of predictive uncertainty, so the reported differences between architectures should be read as observations rather than as a ranking.

Future work will encode the trapping properties as continuous fields derived from the Land coefficient or the maximum residual gas saturation, in order to test whether a band-limited representation preserves both accuracy and transferability; extend the operator to full three-dimensional spectral convolution; and couple the surrogate to a rock-physics and time-lapse seismic monitoring so that saturation and trapped-gas fields can be updated directly from monitoring data.

Acknowledgements

We thank Universiti Teknologi PETRONAS (UTP) for academic and technical support. The Centre for Subsurface Imaging (CSI), UTP, provided the high-performance computing infrastructure (NVIDIA A40 GPUs) used for all model training and inference. We gratefully acknowledge the Computer Modeling Group (CMG) for providing the GEM compositional simulator under academic license. This work was funded by Malaysia-Thailand Joint Authority (MTJA) research project grant (015QA0-044) and YUTP-FRG project grant (015LC0-516, and 015LC0-529).

Funding

This work was supported by the Malaysia-Thailand Joint Authority (MTJA) research project grant (015QA0-044) and by the YUTP-FRG project grants (015LC0-516 and 015LC0-529).

CRediT Authorship Contribution Statement

B. Venkateshwaran: Conceptualization, Methodology, Software, Data curation, Formal analysis, Investigation, Validation, Visualization, Writing – original draft. **AKM Eahsanul Haque:** Supervision, Resources, Writing – review & editing. **Numair Ahmed Siddiqui:** Supervision, Writing – review & editing. **Hariharan Ramachandran:** Supervision, Investigation, Validation, Methodology, Writing – review & editing. **Mu. Ramkumar:** Writing – review & editing. **John Oluwadamilola Olutoki:** Writing – review & editing. **Ida Bagus Suananda Yogi:** Writing – review & editing. **Bamidele Adeniyi:** Writing – review & editing.

Declaration of Competing Interest

The authors declare that they have no known competing financial interests or personal relationships that could have appeared to influence the work reported in this paper.

References

Akbarabadi, M., Piri, M., 2013. Relative permeability hysteresis and capillary trapping characteristics of supercritical CO_2/brine systems: An experimental study at reservoir conditions. Adv. Water Resour. 52, 190–206. https://doi.org/10.1016/j.advwatres.2012.06.014.

Alamara, H., Blondeau, C., Bogdanov, I., 2023. Hysteresis Modelling of Sharp Interface Vertically-Averaged Relative Permeability and Pseudo-Capillary Pressure for Accurate Vertical Equilibrium

Simulation, in: The Fourth EAGE Global Energy Transition Conference and Exhibition. pp. 1–6. https://doi.org/10.3997/2214-4609.202321065.

Alqahtani, A., He, X., Yan, B., Hoteit, H., 2023. Uncertainty analysis of CO_2 storage in deep saline aquifers using machine learning and Bayesian optimization. Energies 16, 4. https://doi.org/10.3390/en16041684.

Altundas, Y.B., Ramakrishnan, T.S., Chugunov, N., de Loubens, R., 2011. Retardation of CO2 caused by capillary pressure hysteresis: A new CO2 trapping mechanism. SPE J. 16, 784–794. https://doi.org/10.2118/139641-PA.

Ashraf, M., Oladyshkin, S., Nowak, W., 2013. Geological storage of CO_2: Application, feasibility and efficiency of global sensitivity analysis and risk assessment using the arbitrary polynomial chaos. Int. J. Greenh. Gas Control 19, 704–719. https://doi.org/10.1016/j.ijggc.2013.03.023.

Bech, N., Frykman, P., 2018. Trapping of buoyancy-driven CO_2 during imbibition. Int. J. Greenhouse Gas Control 78, 48–61. https://doi.org/10.1016/j.ijggc.2018.06.018.

Benson, S.M., Cole, D.R., 2008. CO_2 sequestration in deep sedimentary formations. Elements 4, 325–331. https://doi.org/10.2113/gselements.4.5.325.

Bolourinejad, P., Shoeibi Omrani, P., Herber, R., 2014. Effect of reactive surface area of minerals on mineralization and carbon dioxide trapping in a depleted gas reservoir. Int. J. Greenh. Gas Control 21, 11–22. https://doi.org/10.1016/j.ijggc.2013.11.009.

Brooks, R.H., Corey, A.T., 1964. Hydraulic properties of porous media. Hydrology Papers 3, 1–27.

Bryant, S.L., Lakshiminarasimhan, S., Pope, G.A., 2006. Buoyancy-dominated multiphase flow and its impact on geological sequestration of CO2. SPE J. 13, 447–454. https://doi.org/10.2118/99938-PA.

Burnside, N.M., Naylor, M., 2014. Review and implications of relative permeability of CO_2/brine systems and residual trapping of CO_2. Int. J. Greenh. Gas Control 23, 1–11. https://doi.org/10.1016/j.ijggc.2014.01.013.

Carlson, F.M., 1981. Simulation of relative permeability hysteresis to the nonwetting phase, in: SPE Annual Technical Conference and Exhibition. Society of Petroleum Engineers, San Antonio, TX, SPE-10157. https://doi.org/10.2118/10157-MS.

Chan, C., Nagao, M., Datta-Gupta, A., 2026. Multi-resolution deep learning for accelerated well control optimization in CO_2 storage: A field application at the Illinois Basin Decatur Project (IBDP). Int. J. Greenh. Gas Control 152, 104633. https://doi.org/10.1016/j.ijggc.2025.104633.

Chierici, G.L., 1984. Novel relations for drainage and imbibition relative permeabilities. Society of Petroleum Engineers journal 24, 275–276.

Choubineh, A., Chen, J., Wood, D.A., Coenen, F., Ma, F., 2023. Fourier neural operator for fluid flow in small-shape 2D simulated porous media dataset. Algorithms 16, 1–14. https://doi.org/10.3390/a16010014.

Dance, T., Paterson, L., 2016. Observations of carbon dioxide saturation distribution and residual trapping using core analysis and repeat pulsed-neutron logging at the CO2CRC Otway site. Int. J. Greenhouse Gas Control 47, 210–220. https://doi.org/10.1016/j.ijggc.2016.01.042.

Doster, F., Nordbotten, J.M., Celia, M.A., 2012. Hysteretic upscaled constitutive relationships for vertically integrated porous media flow. Comput. Vis. Sci. 15, 147–161. https://doi.org/10.1007/s00791-013-0205-0.

Doughty, C., Pruess, K., 2004. Modeling supercritical CO2 injection in heterogeneous porous media, in: Proceedings of TOUGH Symposium 2003. Lawrence Berkeley National Laboratory, Berkeley, CA.

Doughty, C., 2007. Modeling geologic storage of carbon dioxide: Comparison of non-hysteretic and hysteretic characteristic curves. Energy Convers. Manag. 48, 1768–1781. https://doi.org/10.1016/j.enconman.2007.01.026.

Duijn, C.J.V., Molenaar, J., De Neef, M.J., 1995. The effect of capillary forces on immiscible two-phase flow in heterogeneous porous media. Transp Porous Media 21, 71–93. https://doi.org/10.1007/BF00615335.

Element, D.J., Masters, J.H.K., Sargent, N.C., Jayasekera, A.J., Goodyear, S.G., 2003. Assesment of three-phase relative permeability models using laboratory hysteresis data, in: SPE International Improved Oil Recovery Conference. Society of Petroleum Engineers, Kuala Lumpur, Malaysia, SPE-84903. https://doi.org/10.2118/84903-MS.

Ershadnia, R., Hajirezaie, S., Amooie, A., Wallace, C.D., Gershenzon, N.I., Hosseini, S.A., Sturmer, D.M., Ritzi, R.W., Soltanian, M.R., 2021. CO_2 geological sequestration in multiscale heterogeneous aquifers: Effects of heterogeneity, connectivity, impurity, and hysteresis. Adv. Water Resour. 151, 103895. https://doi.org/10.1016/j.advwatres.2021.103895.

Feng, Z., Yan, B., Shen, X., Zhang, F., Tariq, Z., Ouyang, W., Han, Z., 2025a. A hybrid CNN-transformer surrogate model for the multi-objective robust optimization of geological carbon sequestration. Adv. Water Resour. 196, 104897. https://doi.org/10.1016/j.advwatres.2025.104897.

Feng, Z., Yan, B., Zhao, L., Shen, X., Zhao, R., Wang, W., Zhang, F., 2025b. SURGIN: SURrogate-guided Generative INversion for subsurface multiphase flow with quantified uncertainty (Version 1). arXiv preprint. https://doi.org/10.48550/ARXIV.2509.13189.

Feng, Z., Tariq, Z., Zhang, Z., Zhao, P., Zhao, R., Wang, W., Huang, X., Yan, B., Shen, X., Zhang, F., 2026. CoSwinNet: A conditional Swin Transformer multimodal surrogate model for subsurface multiphase flow. Fuel 411, 138067. https://doi.org/10.1016/j.fuel.2025.138067.

Frangos, M., Marzouk, Y., Willcox, K., van Bloemen Waanders, B., 2010. Surrogate and reduced-order modeling: A comparison of approaches for large-scale statistical inverse problems. Large-Scale Inverse Probl. Quantif. Uncertainty, 123–149. https://doi.org/10.1002/9780470685853.ch6.

Gal, Y., Koumoutsakos, P., Lanusse, F., Louppe, G., Papadimitriou, C., 2022. Bayesian uncertainty quantification for machine-learned models in physics. Nat. Rev. Phys. 4, 573–577. https://doi.org/10.1038/s42254-022-00488-8.

Geffen, T.M., Owens, W.W., Parrish, D.R., Morse, R.A., 1951. Experimental investigation of factors affecting laboratory relative permeability measurements. Pet. Trans. AIME 192, 99–110. https://doi.org/10.2118/951099-G.

Gershenzon, N.I., Ritzi Jr., R.W., Dominic, D.F., Soltanian, M., Mehnert, E., Okwen, R.T., 2015. Influence of small-scale fluvial architecture on CO2 trapping processes in deep brine reservoirs. Water Resour. Res. 51, 8240–8256. https://doi.org/10.1002/2015wr017638.

Gershenzon, N.I., Ritzi Jr., R.W., Dominic, D.F., Mehnert, E., Okwen, R.T., 2017. Capillary trapping of CO_2 in heterogeneous reservoirs during the injection period. Int. J. Greenh. Gas Control 59, 13–23. https://doi.org/10.1016/j.ijggc.2017.02.002.

Guibas, J., Mardani, M., Li, Z., Tao, A., Anandkumar, A., Catanzaro, B., 2022. Adaptive Fourier neural operators: Efficient token mixers for transformers, in: International Conference on Learning Representations (ICLR 2022).

Han, Y., Hamon, F.P., Jiang, S., Durlofsky, L.J., 2024. Surrogate model for geological CO_2 storage and its use in hierarchical MCMC history matching. Adv. Water Resour. 187, 104678. https://doi.org/10.1016/j.advwatres.2024.104678.

Harris, C., Jackson, S.J., Benham, G.P., Krevor, S., Muggeridge, A.H., 2021. The impact of heterogeneity on the capillary trapping of CO_2 in the Captain Sandstone. Int. J. Greenh. Gas Control 112, 103511. url?id=9.

Herring, A.L., Andersson, L., Wildenschild, D., 2016. Enhancing residual trapping of supercritical CO_2 via cyclic injections. Geophys. Res. Lett. 43, 9677–9685. https://doi.org/10.1002/2016GL070304.

Holtz, M.H., 2002. Residual gas saturation to aquifer influx: A calculation method for 3D computer reservoir model construction, in: SPE Gas Technology Symposium. Society of Petroleum Engineers, SPE-75502-MS. https://doi.org/10.2118/75502-MS.

Hovorka, S.D., Doughty, C., Benson, S.M., Pruess, K., Knox, P.R., 2004. The impact of geological heterogeneity on CO2 storage in brine formations: A case study from the Texas Gulf Coast. Geol. Soc. Spec. Publ. 233, 147–163. https://doi.org/10.1144/GSL.SP.2004.233.01.10.

Ide, S.T., Jessen, K., Orr Jr., F.M., 2007. Storage of CO2 in saline aquifers: Effects of gravity, viscous, and capillary forces on amount and timing of trapping. Int. J. Greenh. Gas Control 1, 481–491. https://doi.org/10.1016/S1750-5836(07)00091-6.

Iglauer, S., Pentland, C.H., Busch, A., 2015. CO2 wettability of seal and reservoir rocks and the implications for carbon geo-sequestration. Water Resour. Res. 51, 729–774. https://doi.org/10.1002/2014WR015553.

Jackson, S., Lin, Q., Krevor, S., 2020a. Representative elementary volumes, hysteresis and heterogeneity in multiphase flow from the pore to continuum scale. Water Resour Res 1–33. https://doi.org/10.1029/2019wr026396.

Jackson, S.J., Agada, S., Reynolds, C.A., Krevor, S., 2018. Characterizing drainage multiphase flow in heterogeneous sandstones. Water Resour Res 54, 3139–3161. https://doi.org/10.1029/2017WR022282.

Jackson, S.J., Krevor, S., 2020b. Small-scale capillary heterogeneity linked to rapid plume migration during CO2 storage. Geophys Res Lett. https://doi.org/10.1029/2020GL088616

Jerauld, G., Salter, S., 1990. The effect of pore-structure on hysteresis in relative permeability and capillary pressure: pore-level modeling. Transp Porous Media 5, 103–151.

Jerauld, G.R., 1997. General three-phase relative permeability model for Prudhoe Bay. SPE Reserv. Eng. 12, 255–263. https://doi.org/10.2118/36178-PA.

Jettestuen, E., Helland, J.O., Prodanović, M., 2013. A level set method for simulating capillary-controlled displacements at the pore scale with nonzero contact angles. Water Resour. Res. 49, 4645–4661. https://doi.org/10.1002/wrcr.20334.

Jettestuen, E., Friis, H.A., Helland, J.O., 2021. A locally conservative multiphase level set method for capillary-controlled displacements in porous media. J. Comput. Phys. 428, 109965. https://doi.org/10.1016/j.jcp.2020.109965.

Jettestuen, E., Aursjø, O., Helland, J., Vinningland, J., Hiorth, A., 2024. Workflow for direct pore-scale simulation of relative permeability and capillary pressure curves with hysteresis at low capillary numbers, in: SPE Norway Subsurface Conference. Society of Petroleum Engineers, pp. 011–010001. https://doi.org/10.2118/218413-MS.

Jiang, Z., Zhu, M., Li, D., Li, Q., Yuan, Y.O., Lu, L., 2023. Fourier-MIONet: Fourier-enhanced multiple-input neural operators for multiphase modeling of geological carbon sequestration. arXiv preprint arXiv:2303.04778. https://doi.org/10.48550/arXiv.2303.04778.

Jin, L., Pekot, L.J., Smith, S.A., et al., 2018. Effects of gas relative permeability hysteresis and solubility on associated CO2 storage performance. Int. J. Greenh. Gas Control 75, 140–150. https://doi.org/10.1016/j.ijggc.2018.06.002.

Juanes, R., Spiteri, E.J., Orr Jr., F.M., Blunt, M.J., 2006. Impact of relative permeability hysteresis on geological CO2 storage. Water Resour. Res. 42, 1. https://doi.org/10.1029/2005WR004806.

Kaufmann, R., Aavatsmark, I., Nøkleby, P.H., Aurdal, T.A., 2016. Using an aquifer as CO_2 buffer storage. Int. J. Greenh. Gas Control 53, 106–116. https://doi.org/10.1016/j.ijggc.2016.07.037.

Killough, J.E., 1976. Reservoir simulation with history-dependent saturation functions. Soc. Pet. Eng. J. 16, 37–48. https://doi.org/10.2118/5106-PA.

Kovachki, N., Li, Z., Liu, B., Azizzadenesheli, K., Bhattacharya, K., Stuart, A., Anandkumar, A., 2023. Neural operator: Learning maps between function spaces with applications to PDEs. J. Mach. Learn. Res. 24, 1–97.

Krevor, S., Blunt, M.J., Benson, S.M., Pentland, C.H., Reynolds, C., Al-Menhali, A., Niu, B., 2015. Capillary trapping for geologic carbon dioxide storage – From pore scale physics to field scale implications. Int. J. Greenh. Gas Control 40, 221–237. https://doi.org/10.1016/j.ijggc.2015.06.013.

Krevor, S.C., Pini, R., Li, B., Benson, S.M., 2011. Capillary heterogeneity trapping of CO_2 in a sandstone rock at reservoir conditions. Geophys Res Lett 38, 1–5. https://doi.org/10.1029/2011GL048239.

Krevor, S.C., Pini, R., Zuo, L., Benson, S.M., 2012. Relative permeability and trapping of CO_2 and water in sandstone rocks at reservoir conditions. Water Resour Res 48, 1–16. https://doi.org/10.1029/2011WR010859.

Kumar, A., Ozah, R., Noh, M., Pope, G.A., Bryant, S., Sepehrnoori, K., Lake, L.W., 2005. Reservoir simulation of CO2 storage in deep saline aquifers. SPE J. 10, 336–348. https://doi.org/10.2118/89343-pa.

Lan, Y., Guo, P., Liu, Y., Wang, S., Cao, S., Zhang, J., Sun, W., Qi, D., Ji, Q., 2024. State of the art on relative permeability hysteresis in porous media: Petroleum engineering application. Appl. Sci. 14, 4639. https://doi.org/10.3390/app14114639.

Land, C.S., 1968. Calculation of imbibition relative permeability for two- and three-phase flow from rock properties. Soc. Pet. Eng. J. 8, 149–156. https://doi.org/10.2118/1942-PA.

Leverett, M., 1940. Capillary behavior in porous solids. Petroleum Technology 152–169. https://doi.org/10.2118/941152-G.

Li, Z., Kovachki, N., Azizzadenesheli, K., Liu, B., Bhattacharya, K., Stuart, A., Anandkumar, A., 2021. Fourier neural operator for parametric partial differential equations, in: International Conference on Learning Representations (ICLR 2021).

Lun, L., Szafranski, R., 2023. Developing Consistent Relative Permeability and Capillary Pressure Models for Reservoir Simulation of CCS Projects, in: EAGE Workshop on Unlocking Carbon Capture and Storage Potential. pp. 1–3. https://doi.org/10.3997/2214-4609.202374010.

Mao, S., Carbonero, A., Mehana, M., 2025. Deep learning for subsurface flow: A comparative study of U-Net, Fourier neural operators, and transformers in underground hydrogen storage. J. Geophys. Res. Mach. Learn. Comput. https://doi.org/10.1029/2024JH000213.

Moghadasi, R., Foroughi, S., Goodarzi, S., Zhang, Y., Bijeljic, B., Blunt, M.J., Niemi, A., 2025. Trapping and remobilization during geological CO_2 storage: A pore-scale imaging and modeling study. Adv. Water Resour. 205, 105092. https://doi.org/10.1016/j.advwatres.2025.105092.

Møll Nilsen, H., Lie, K.A., Andersen, O., 2015. Analysis of CO_2 trapping capacities and long-term migration for geological formations in the Norwegian North Sea using MRST-co2lab. Comput. Geosci. 79, 15–26. https://doi.org/10.1016/j.cageo.2015.03.008.

Newell, D.L., Kaszuba, J.P., Viswanathan, H.S., Pawar, R.J., Carpenter, T., 2008. Significance of carbonate buffers in natural waters reacting with supercritical CO_2: Implications for monitoring, measuring and verification (MMV) of geologic carbon sequestration. Geophys. Res. Lett. 35, 1–5. https://doi.org/10.1029/2008GL035615.

Ni, H., Boon, M., Garing, C., Benson, S.M., 2019. Predicting CO_2 residual trapping ability based on experimental petrophysical properties for different sandstone types. Int. J. Greenh. Gas Control 86, 158–176. https://doi.org/10.1016/j.ijggc.2019.04.024.

Ni, H., Møyner, O., Kurtev, K.D., Benson, S.M., 2021. Quantifying CO2 capillary heterogeneity trapping through macroscopic percolation simulation. Adv. Water Resour. 155, 103990. https://doi.org/10.1016/j.advwatres.2021.103990.

Nilsen, H.M., Lie, K.A., Andersen, O., 2016. Fully-implicit simulation of vertical-equilibrium models with hysteresis and capillary fringe. Comput. Geosci. 20, 49–67. https://doi.org/10.1007/s10596-015-9549-0.

Nooruddin, H.A., Hossain, M.E., 2011. Modified Kozeny-Carman correlation for enhanced hydraulic flow unit characterization. J. Pet. Sci. Eng. 80, 107–115. https://doi.org/10.1016/j.petrol.2011.11.002.

Obi, E.-O.I., Blunt, M.J., 2006. Streamline-based simulation of carbon dioxide storage in a North Sea aquifer. Water Resour. Res. 42, W03414. https://doi.org/10.1029/2004WR003347.

Osoba, J.S., Richardson, J.G., Kerver, J.K., Hafford, J.A., Blair, P.M., 1951. Laboratory measurements of relative permeability. Pet. Trans. AIME 192, 47–56. https://doi.org/10.2118/951047-G.

Patel, H.S., Meher, R., 2017. Modelling of imbibition phenomena in fluid flow through heterogeneous inclined porous media with different porous materials. Nonlinear Eng. 6, 263–275. https://doi.org/10.1515/nleng-2017-0010.

Pini, R., Krevor, S.C.M., Benson, S.M., 2012. Capillary pressure and heterogeneity for the CO_2/water system in sandstone rocks at reservoir conditions. Adv. Water Resour. 38, 48–59. https://doi.org/10.1016/j.advwatres.2011.12.007.

Pini, R., Benson, S.M., 2017. Capillary pressure heterogeneity and hysteresis for the supercritical CO_2/water system in a sandstone. Adv. Water Resour. 108, 277–292. https://doi.org/10.1016/j.advwatres.2017.08.007.

Rasmusson, K., Rasmusson, M., Tsang, Y., Benson, S., Hingerl, F., Fagerlund, F., Niemi, A., 2018. Residual trapping of carbon dioxide during geological storage—Insight gained through a pore-network modeling approach. Int. J. Greenh. Gas Control 74, 62–78. https://doi.org/10.1016/j.ijggc.2018.04.013.

Ren, J., Wang, Y., Feng, D., Gong, J., 2021. CO_2 migration and distribution in multiscale-heterogeneous deep saline aquifers. Adv. Geo-Energy Res. 5, 333–346. https://doi.org/10.46690/ager.2021.03.07.

Reynolds, C.A., Krevor, S., 2015. Characterizing flow behavior for gas injection: relative permeability of CO_2-brine and N_2-water in heterogeneous rocks. Water Resour Res 51, 9464–9489. https://doi.org/10.1002/2015WR018046.

Reynolds, C.A., Blunt, M.J., Krevor, S., 2018. Multiphase flow characteristics of heterogeneous rocks from CO_2 storage reservoirs in the United Kingdom. Water Resour Res 54, 729–745. https://doi.org/10.1002/2017WR021651.

Ruprecht, C., Pini, R., Falta, R., Benson, S., Murdoch, L., 2014. Hysteretic trapping and relative permeability of CO_2 in sandstone at reservoir conditions. Int. J. Greenh. Gas Control 27, 15–27. https://doi.org/10.1016/j.ijggc.2014.05.003.

Saadatpoor, E., Bryant, S.L., Sepehrnoori, K., 2009. Effect of capillary heterogeneity on buoyant plumes: A new local trapping mechanism. Energy Procedia 1, 3299–3306. https://doi.org/10.1016/j.egypro.2009.02.116.

Spiteri, E.J., Juanes, R., 2006. Impact of relative permeability hysteresis on the numerical simulation of WAG injection. J. Pet. Sci. Eng. 50, 115–139. https://doi.org/10.1016/j.petrol.2005.08.006.

Sun, Z., Xu, J., Espinoza, D.N., Balhoff, M.T., 2021. Optimization of subsurface CO_2 injection based on neural network surrogate modeling. Comput. Geosci. 25, 1887–1898. https://doi.org/10.1007/s10596-021-10086-y.

Tahmasebi, P., Kamrava, S., Bai, T., Sahimi, M., 2020. Machine learning in geo- and environmental sciences: From small to large scale. Adv. Water Resour. 142, 103619. https://doi.org/10.1016/j.advwatres.2020.103619.

Tang, H., Fu, P., Sherman, C.S., Zhang, J., Ju, X., Hamon, F., Burton-Kelly, N.A., Azzolina, N.A., Morris, J.P., 2021. A deep learning-accelerated data assimilation and forecasting workflow for commercialscale geologic carbon storage. Int. J. Greenh. Gas Control 112, 103488. https://doi.org/10.1016/j.ijggc.2021.103488.

Tang, M., Ju, X., Durlofsky, L.J., 2022. Deep-learning-based coupled flow-geomechanics surrogate model for CO_2 sequestration. Int. J. Greenh. Gas Control 118, 103692. https://doi.org/10.1016/j.ijggc.2022.103692.

Tariq, Z., Feng, Z., Hoteit, H., Abualsaud, M., He, X., AlMajid, M., Sun, S., Yan, B., 2024. TransUNet: Accelerating Multiphase Flow Prediction in Geological Carbon Storage Systems, in: ADIPEC. Society of Petroleum Engineers, SPE-222334-MS. https://doi.org/10.2118/222334-ms.

Wen, G., Hay, C., Benson, S.M., 2021a. CCSNet: A deep learning modeling suite for CO_2 storage. Adv. Water Resour. 155, 104009. https://doi.org/10.1016/j.advwatres.2021.104009.

Wen, G., Tang, M., Benson, S.M., 2021b. Towards a predictor for CO_2 plume migration using deep neural networks. Int. J. Greenh. Gas Control 105, 103223. https://doi.org/10.1016/j.ijggc.2020.103223.

Wen, G., Li, Z., Azizzadenesheli, K., Anandkumar, A., Benson, S.M., 2022. U-FNO—An enhanced Fourier neural operator-based deep-learning model for multiphase flow. Adv. Water Resour. 163, 104180. https://doi.org/10.1016/j.advwatres.2022.104180.

Wen, G., Li, Z., Long, Q., Azizzadenesheli, K., Anandkumar, A., Benson, S.M., 2023. Real-time high-resolution CO_2 geological storage prediction using nested Fourier neural operators. Energy Environ. Sci. 16, 1732–1741. https://doi.org/10.1039/D2EE03457A.

Werner, M., Sutter, D., Krättli, A., Lafci, Ö., Mutschler, R., Oehler, P., Winkler, J., Mazzotti, M., 2014. A physical model for geological CO_2 storage - Replacing misconceptions by visual explanation. Int. J. Greenh. Gas Control 25, 42–53. https://doi.org/10.1016/j.ijggc.2014.04.004.

Witte, P.A., Konuk, T., Skjetne, E., Chandra, R., 2023. Fast CO_2 saturation simulations on large-scale geomodels with artificial intelligence-based wavelet neural operators. Int. J. Greenh. Gas Control 126, 103880. https://doi.org/10.1016/j.ijggc.2023.103880.

Xiao, C., Zhang, S., Ma, X., Zhou, T., Hou, T., Chen, F., 2023. Deep-learning-generalized data-space inversion and uncertainty quantification framework for accelerating geological CO_2 plume migration monitoring. Geoenergy Sci. Eng. 224, 211627. https://doi.org/10.1016/j.geoen.2023.211627.

Yan, B., Chen, B., Harp, D.R., Jia, W., Pawar, R.J., 2022. A robust deep learning workflow to predict multiphase flow behavior during geological CO_2 sequestration injection and post-injection periods. J. Hydrol. 607, 127542. https://doi.org/10.1016/j.jhydrol.2022.127542.

Yin, Z., Louboutin, M., Møyner, O., Herrmann, F.J., 2025. Time-lapse full-waveform permeability inversion: A feasibility study. 544–553.

Zahasky, C., Benson, S.M., 2014. A simple approximate semi-analytical solution for estimating leakage of carbon dioxide through faults. Energy Procedia 63, 4861–4874. https://doi.org/10.1016/j.egypro.2014.11.517.

Zhu, S., Sun, J., Wei, G., et al., 2021. Numerical simulation-based correction of relative permeability hysteresis in water-invaded underground gas storage during multicycle injection and production. Pet. Explor. Dev. 48, 190–200. https://doi.org/10.1016/S1876-3804(21)60015-0.